

Inverse Analysis of Experimental Scale Turbidity Currents Using Deep Learning Neural Networks

Zhirong Cai^{1*}, Hajime Naruse¹

¹Kyoto University

Key Points:

- Inverse analysis of turbidity currents using deep learning neural networks was performed for experimental scale turbidites.
- Inverse analysis results for numerical datasets proved that flow conditions can be reconstructed from characteristics of deposits.
- Flow conditions and deposit profiles in flume experiments were also well reconstructed.

*Kyoto, Japan

Corresponding author: Zhirong Cai, cai.zhirong.64w@kyoto-u.jp

Abstract

Despite the importance of turbidity currents in environmental and resource geology, their flow conditions and mechanisms are not well understood. This study proposes a novel method for the inverse analysis of turbidity currents using a deep learning neural network (DNN) to better explore the properties of turbidity currents. The aim of this study is to verify the DNN inverse method using numerical and flume experiment datasets. Numerical datasets of turbidites were generated with a forward model. Then, the DNN model was trained to find the functional relationship between flow conditions and turbidites by processing the numerical datasets. The performance of the trained DNN model was evaluated with 2000 numerical test datasets and 5 experiment datasets. Inverse analysis results on numerical test datasets indicated that flow conditions can be reconstructed from depositional characteristics of turbidites. For experimental turbidites, spatial distributions of grain size and thickness were consistent with the samples values. Concerning hydraulic conditions, flow depth H , layer-averaged velocity U , and flow duration T_d were reconstructed with a certain level of deviation. Greater discrepancies between the measured and reconstructed values of flow concentration were observed relative to the former three parameters (H , U , T_d), which may be attributed to difficulties in measuring the flow concentration during experiments. The precision of the reconstructions for experimental datasets was estimated using Jackknife resampling. Although the DNN model did not provide perfect reconstruction, it proved to be a significant advance for the inverse analysis of turbidity currents.

Plain Language Summary

This study performed inverse analysis on turbidity currents using a machine learning method. Flume experiments were conducted to verify the method. Turbidite, the deposit of turbidity current, is an active area of study because it is closely related to the exploration of petroleum resources. Since turbidites are often deposited as a result of tsunami events, the understanding of turbidity currents can also contribute to geohazard prevention. The inverse analysis method proposed in this study can help enhance our understanding of the flow properties of turbidity currents.

1 Introduction

A turbidity current is a process of sediment transport into subaqueous environments such as deep lakes and oceans (Daly, 1936; Johnson, 1939). Turbidites, the deposits of turbidity currents, are often characterized by graded bedding and sedimentary successions called the Bouma sequence (e.g., Kuenen & Migliorini, 1950; Bouma, 1962; Talling et al., 2012). Turbidites have been an active area of study due to their close association with petroleum resources and their role in the destruction of sea-floor equipment, such as submarine cables (Weimer & Slatt, 2007; Talling et al., 2015). Furthermore, turbidites are often deposited as a result of tsunami triggered turbidity currents (Arai et al., 2013) and thus can contribute to determine the recurrence intervals of geohazards.

Studying the flow behavior of turbidity currents is essential for understanding the characteristics of turbidites and their implications (Talling et al., 2007). However, knowledge in this area remains limited because of difficulties in the direct observation of turbidity currents. Several in-situ measurements have been conducted (e.g., Xu et al., 2004; Vangriesheim et al., 2009; Arai et al., 2013; Paull et al., 2018) and extensive research detailing the dynamics of the measured flows was conducted (e.g., Chikita, 1989; Dorrell et al., 2016; Azpiroz-Zabala et al., 2017; Heerema et al., 2020; Simmons et al., 2020). However, measurements of hydraulic conditions, such as sediment concentration, were difficult because of the destructive nature and unpredictable occurrences of turbidity currents (Naruse & Olariu, 2008; Falcini et al., 2009; Lesshafft et al., 2011; Talling et al., 2015). Recently, Simmons et al. (2020) proposed a novel acoustic method for measuring the concentration structure within submarine turbidity currents. The method was able to extract the sediment concentration data from ADCP measurements, but did not perform well at high concentrations. The method also assumed a single grain-size class in flow, which is not consistent with actual flow in nature. Therefore, inverse analysis that reconstructs the flow conditions of turbidity currents from their deposits is crucial for estimating the flow conditions in natural environments.

Before this research, inverse analysis of turbidity currents was conducted by Baas et al. (2000), where flow velocity was reconstructed through analyses of sedimentary structures of turbidites. The results provided an estimation of the hydraulic conditions of flow at a single location, but did not provide a reconstruction of the spatial evolution of the turbidity current. In contrast, inverse analysis methods in previous studies based on numerical models provided more detailed insights into the spatial structure and evolution of flows over time (e.g., Falcini et al., 2009; Lesshafft et al., 2011; Parkinson et al., 2017). The method proposed by Falcini et al. (2009) assumed steady flow conditions and was simplified for obtaining analytical solutions, preventing it from accurately illustrating the flow mechanism of unsteady turbidity currents that can produce normally graded bedding. Consequently, this method cannot be applied to normally graded beds, which are typical characteristics of turbidites. Other studies used the optimization method, where the hydraulic parameters were determined by optimizing the input parameters of numerical models, so that the resulting calculations were consistent with the observed data from turbidites (Lesshafft et al., 2011). This method can provide a relatively good reconstruction of the hydraulic conditions of turbidity currents, but has an extremely heavy calculation load due to the complexity of the forward model employed and the repetitive calculation of the forward model for optimization. Therefore, applying the method to natural scale turbidites, which typically run over tens to hundreds of kilometers and flow continuously for several hours (Talling et al., 2015), is impossible. Optimization using the adjoint approach proposed by Parkinson et al. (2017) solved the problem of heavy calculation load, but the reconstructed values differed from the expected values up to an order of magnitude.

Since previous methods to estimate flow conditions for turbidites were either overly simplified (Baas et al., 2000), incapable of reproducing graded beds (Falcini et al., 2009), accurate but computationally intractable for natural scale turbidity currents (Lesshafft et al., 2011), or low in accuracy (Parkinson et al., 2017), a method that is both accurate and not computationally intractable should be developed. To resolve the aforementioned issues, Naruse and Nakao (2020) proposed a new method for inverse analysis of turbidite deposits using deep learning neural networks (DNN). A DNN model is a machine-learning computing system that works as a universal function approximator (Liang & Srikant, 2016), meaning that an unknown function governing the relationship between observations within a domain is explored and approximated. Previously, it was applied to problems such as landslide susceptibility analyses (Pradhan et al., 2010) and identification of lithology from well log data (Rogers et al., 1992), where the empirical relationship between the observed data and parameters aimed to be predicted was explored. In the case of turbidity currents, however, it is impossible to obtain sufficient datasets of in-situ measurements of flow characteristics for developing a DNN inverse model. Instead of using in-situ measurements of turbidity currents in nature, Naruse and Nakao (2020) generated numerical datasets of turbidites using a forward model. The generated datasets were input into a DNN model to explore the functional relationship between turbidites and initial flow conditions. After this network training process, the DNN model can estimate flow conditions from new turbidite data. Naruse and Nakao (2020) performed inverse analysis using a trained DNN model on field scale numerical test datasets generated by a forward model. Their results showed that the DNN model can reconstruct flow properties from numerical test datasets and was robust against noise in input data. Although the DNN model has demonstrated its performance on numerical datasets, it has yet to be tested with turbidite data from experiments or in-situ measurements.

In this study, we verified the ability of the DNN model to perform inverse analysis of turbidity currents by applying it to data collected from turbidites deposited in flume experiments. We chose to first test the DNN inverse model on flume experiments instead of field data, because turbidity currents were generated in a controlled environment during flume experiments. Conditions, including flow duration and initial hydraulic conditions, can be set manually, and measurements of these parameters can also be conducted easily during experiments.

Here, we implemented a forward model and a DNN inverse model. The forward model was implemented with the same governing equations as Naruse and Nakao (2020), but the numerical scheme and closure equations were modified to accommodate experimental scale simulations and improve the accuracy of the calculation. The DNN model was trained with the experimental scale numerical datasets. The trained DNN model was first tested with independent sets of numerical datasets that were also produced by the forward model. Then, the trained DNN model was tested with flume experiment data. Initial flow conditions of experiments were reconstructed from sampled deposits. These flow conditions were then fed into the forward model to reconstruct the spatio-temporal evolution of the experiment. Reconstructed hydraulic conditions during the flow and grain size distribution of the deposits were compared with the measured values.

2 Forward Model

2.1 Governing Equations

The forward model implemented in this study is a layer-averaged shallow water model based on Kostic and Parker (2006). It is expanded to account for the transport and deposition of non-uniform grain size distribution discretized to multiple grain-size classes in Nakao et al. (2020) (Figure 1). This model was chosen because it is

sufficiently complex to some details of the internal structure of flow, but also contains simplifications that make its calculation cost reasonable. The five governing equations are as follows:

$$\frac{\partial H}{\partial t} + U \frac{\partial H}{\partial x} = e_w U - H \frac{\partial U}{\partial x}, \quad (1)$$

$$\frac{\partial U}{\partial t} + U \frac{\partial U}{\partial x} = RC_T g (\sin \theta - \cos \theta \frac{\partial H}{\partial x}) - \frac{1}{2} g H R \cos \theta \frac{\partial C_T}{\partial x} - \frac{U^2}{H} (c_f - e_w), \quad (2)$$

$$\frac{\partial C_i}{\partial t} + U \frac{\partial C_i}{\partial x} = \frac{w_i}{H} (F_i e_{si} - r_o C_i) - \frac{e_w C_i U}{H}, \quad (3)$$

$$\frac{\partial \eta_i}{\partial t} = \frac{w_i}{1 - \lambda_p} (r_o C_i - e_{si} F_i), \quad (4)$$

$$\frac{\partial F_i}{\partial t} + \frac{F_i}{L_a} \frac{\partial \eta_T}{\partial t} = \frac{w_i}{L_a (1 - \lambda_p)} (r_o C_i - e_{si} F_i), \quad (5)$$

where the equations represent fluid mass conservation (equation 1), momentum conservation (equation 2), sediment mass conservation (equation 3), mass conservation in bed (Exner's equation) (equation 4), and sediment mass conservation in active layer (equation 5) (Nakao et al., 2020).

Let x and t be the bed-attached streamwise coordinate and time, respectively. Parameters H , U , and C_i represent the flow depth, the layer-averaged velocity, and the layer-averaged volumetric concentration of suspended sediment of the i th grain-size class, respectively. In this study, the number of grain-size classes and representative grain diameters were determined on the basis of the grain size distribution in each experiment (specific values noted in Section 5.1). Parameter C_T denotes the layer-averaged total concentration of suspended sediment ($C_T = \sum C_i$), and g represents gravitational acceleration. Parameter c_f is the friction coefficient. Parameter θ is the angle of inclination of the base slope. Sediment properties are described by R , the submerged specific density of sediment; w_i represents the settling velocity of a sediment particle of the i th grain-size class; λ_p represents the porosity of bed sediment. Parameter η_i is the volume per unit area of bed sediment of the i th grain-size class, and η_T is the sum of all η_i ($\eta_T = \sum \eta_i$). Parameters L_a represents the active layer thickness, and F_i represents the volume fraction of the i th grain-size class in active layer. Parameters e_{si} , e_w , and r_o represent the entrainment rate of sediment of the i th grain-size class into suspension, the entrainment rate of ambient water to flow, and the ratio of near-bed suspended sediment concentration to the layer-averaged concentration of suspended sediment, respectively (Figure 1).

2.2 Closure Equations

Empirical formulations from previous studies are adapted to close the governing equations. In this study, the friction coefficient c_f is assumed to be a constant value. The particle settling velocity w_i for each grain-size class with a representative grain diameter D_i is calculated using the relation from Dietrich (1982), which can be expressed as follows:

$$w_i = R_{fi} \sqrt{RgD_i}, \quad (6)$$

$$R_{fi} = \exp(-b_1 + b_2 \log(Re_{pi}) - b_3 (\log(Re_{pi}))^2 - b_4 (\log(Re_{pi}))^3 + b_5 (\log(Re_{pi}))^4), \quad (7)$$

$$Re_{pi} = \frac{\sqrt{RgD_i} D_i}{\nu}, \quad (8)$$

where b_1 , b_2 , b_3 , b_4 and b_5 are 2.891394, 0.95296, 0.056835, 0.000245 and 0.000245, respectively. e_w is calculated using the empirical formula from Fukushima et al. (1985) as follows:

$$e_w = \frac{0.00153}{0.0204 + Ri}, \quad (9)$$

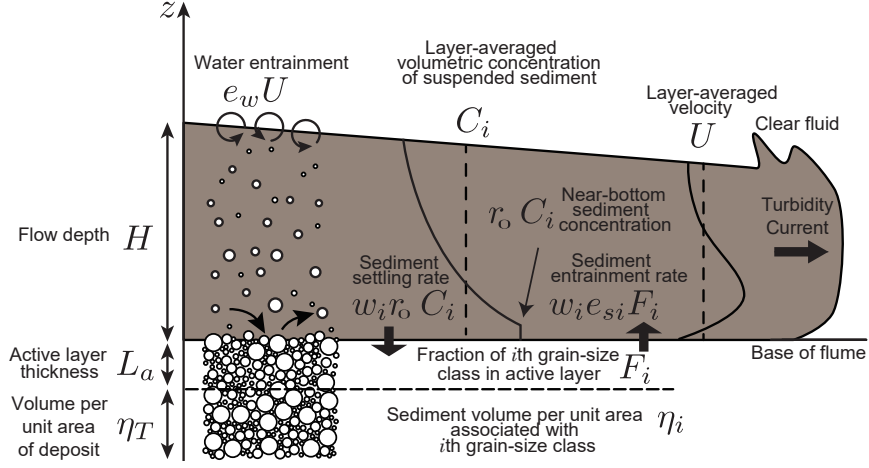


Figure 1. Schematic diagram of processes considered in the forward model from Nakao et al. (2020).

with Ri , the bulk Richardson number, defined as:

$$Ri = \frac{RgC_T H}{U^2}. \quad (10)$$

The entrainment coefficient of sediment e_s is calculated using the empirical relation from Garcia and Parker (1993):

$$e_{si} = \frac{aZ^5}{1 + (a/0.3)Z^5}, \quad (11)$$

$$Z = \alpha_1 \frac{u_*}{w_i} Re_p^{\alpha_2}, \quad (12)$$

where shear velocity u_* is calculated as follows:

$$u_* = \sqrt{c_f} U, \quad (13)$$

and the constants α_1 and α_2 are 0.586 and 1.23 respectively if $Re_p \leq 2.36$. If $Re_p > 2.36$, α_1 and α_2 are 1.0 and 0.6, respectively. Constant a is 1.3×10^{-7} . Kinematic viscosity of water ν is calculated as follows:

$$\nu = \mu/\rho, \quad (14)$$

where ρ and μ denote water density and dynamic viscosity, respectively. The experimentally determined values for μ at 20.0°C (Rumble, 2018) were used in the calculation of ν in this study.

2.3 Implementation of Forward Model

In this study, the constrained interpolation profile (CIP) method (Yabe et al., 2001) implemented with staggered grid was used for integrating of the partial differential equations 1, 2, and 3. The stability condition of the CIP scheme is as follows (Gunawan, 2015):

$$1 > \frac{\Delta t \max(|U| + \sqrt{gH})}{\Delta x}. \quad (15)$$

In this study, the time step Δt was fixed to a value of 0.01 s so that it does not violate the stability condition. The CIP scheme implemented was of third order accuracy. Although this numerical scheme is not strictly mass-conservative, the volume loss of this method has been verified to be less than 0.07% when tested with a simple numerical wave tank (NWT), acceptable for fluid simulation (Vestbøstad et al., 2007). To stabilize the calculation, artificial viscosity was used with the scheme of Jameson et al. (1981), where the parameter κ was set to 0.25. The two-step Adams predictor-corrector method, which was more stable than the ordinary Euler's method, was used to solve ordinary differential equations 4 and 5. Interval of spatial grids Δx was set to 0.05 m based on experimental settings (Section 4.1). The model was tested with different mesh sizes ranging from one fifth to five times the current mesh size and was confirmed to be mesh independent. Initial values of θ for all grids were set to the same value as the base slope of experimental setups.

The Dirichlet boundary condition was used for the upstream boundary, where all flow parameters at the upper boundary of the calculation domain, including the initial flow depth H_0 , the initial flow velocity U_0 , the initial total volumetric concentration of sediment $C_{T,0}$, and the initial volumetric concentration of each grain-size class $C_{i,0}$, were set to be constant. Parameter $F_{i,0}$, the initial volume fraction of the i th grain-size class in active layer, was set to $1/N$ for all grain-size classes, where N represents the number of grain-size classes. The downstream boundary was the Neumann boundary condition in which all parameters were set to the same values as those of the grid adjacent to the lower boundary toward the upstream direction. Other than the upstream boundary, all flow parameters were initialized to zero. The wet-dry boundary condition at the head of the flow was conducted using the scheme proposed by Yang et al. (2016). A threshold value of $C_T H$, ϵ , was used to determine the position of the waterfront. If $C_T H < \epsilon$, the grid was dry. If $C_T H \geq \epsilon$, the grid was wet. In this study, ϵ was set to 0.000001. A dry grid adjacent and downstream to a wet grids was a partial wet grid. Flow discharge M at a partial wet grid j was calculated using Homma's equation (Yang et al., 2016) as follows:

$$M = C_s H_{j-1} \sqrt{R g C_{T,j-1} H_{j-1}}, \quad (16)$$

where C_s , the discharge coefficient, is equal to 0.35.

The density of the surrounding fluid ρ was set to 1000.0 kg/m³ in this study, since experiments were conducted with water. The submerged specific density of sediment $R = (\rho_s - \rho)/\rho$ was set differently according to the types of particles used in experiments (ρ_s is the density of sediment particles), which are stated in Section 4.1. The porosity of bed sediment λ_p was assumed to be 0.4. In this study, both the friction coefficient c_f and ratio of near-bed concentration to layer-averaged values r_o were assumed to be constant. c_f was set to 0.004. r_o was set to 1.5 (Kostic & Parker, 2006). In addition, the thickness of active layer L_a was set to be a constant, 0.003 m (Arai et al., 2013). The gravitational acceleration g was 9.81 m/s².

3 Inverse Analysis by Deep Learning Neural Network

In this method, initial flow conditions of turbidity currents are reconstructed from their turbidite deposits. The DNN model first explores the functional relationship between the initial flow conditions of turbidity currents and the resulting turbidite deposits via training. After training, the DNN model is applied to new turbidite datasets for inverse analysis. In preparation for training, numerical training datasets are generated using the forward model. During training, the training datasets are fed into the DNN. The DNN model examines the datasets and adjusts its internal parameters to make a good estimation of the initial flow conditions from the deposit profile. After training, the DNN, which is can predict the initial flow conditions of new turbidites based on the functional relationship it discovered, is tested with independent numeri-

cal datasets that are also generated by the forward model and with flume experiment data. The procedure of using the DNN model as a method of inverse analysis in this study is illustrated in a flowchart in Figure 2.

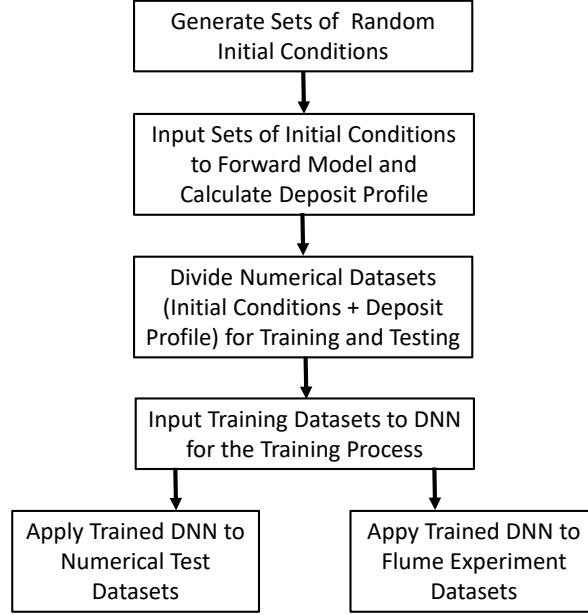


Figure 2. A flowchart illustrating the procedures from generation of numerical data to the application of a DNN model to numerical test datasets and flume experiment datasets.

3.1 Generation of Training Data

A training dataset is a combination of randomly generated initial flow conditions at the upstream boundary of the flow and a matching deposit profile calculated using the forward model. A program in Python was written to generate sets of initial flow conditions. Each set of flow conditions generated consists of an initial flow velocity U_0 , an initial flow depth H_0 , a flow duration T_d , and the initial concentrations of each grain-size class $C_{i,0}$. Other variables, such as slope, are set to constant values. The slope was set according to values of slope in experiments conducted (Section 4.1).

The forward model calculates the deposit profile of a turbidite using randomly generated initial flow conditions. The deposit profile is calculated as volume per unit area for each grain-size class at 60 locations within a 3 m range downstream from the upstream boundary. Each data point is 0.05 m away from its neighboring points. These data points are akin to sampled data from flume experiments or core or outcrop data from actual turbidites. Since fewer data points can be obtained from experiments or actual turbidites, details of deposit profiles need to be interpolated from available data points. Table 1 illustrates the ranges of randomly generated initial flow conditions. These ranges were decided on the basis of possible values that can be observed in experimental scale turbidity currents. Since terms in the forward model calculation were set to be consistent with experimental settings instead of natural scale turbidity currents, no range of values beyond that of experimental scale would be appropriate for the current model implemented. In this study, 10000 training datasets were used for training and 2000 datasets were used for verifying the DNN. The number of test datasets was chosen to be the same number as that of validation datasets. The test

numerical datasets for verification were generated independently from the training datasets.

Table 1. Range of initial flow conditions generated for the generating of training datasets.

Parameter	Minimum	Maximum
H_0 (m)	0.01	0.3
U_0 (m/s)	0.01	0.2
$C_{i,0}$	0.0002	0.005
T_d (s)	180	1080

3.2 Structure of Deep Learning Neural Network

The type of neural network (NN) used in this study is a fully connected NN, which consists of an input layer, several hidden layers, and an output layer. Each layer consists of some nodes. Each node connects with every node in the adjacent layers (Figure 3A). Nodes in the input layer hold deposit profile values, i.e., the volume-per-unit-area for all grain-size classes at spatial grids. Nodes in the output layer hold estimates of parameters we seek to reconstruct, which in this case are the initial flow conditions U_0 , H_0 , $C_{i,0}$, and the flow duration T_d . The activation function used in this study is the rectified linear unit (ReLU), which is one of the most commonly used activation functions for DNNs and is proven to perform calculations at a higher speed than other activation functions (Krizhevsky et al., 2012).

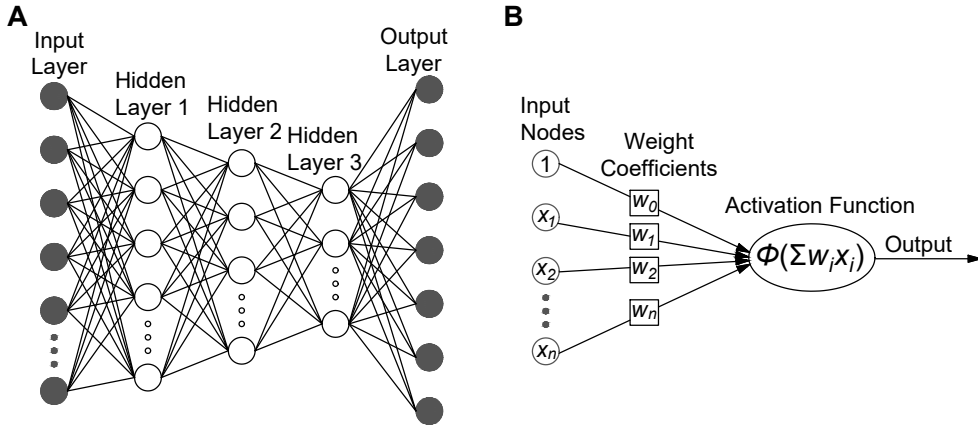


Figure 3. Schematic diagrams of DNN. A. Overall structure of DNN. B. Concept of weight coefficient and activation function.

Before training, the weight coefficients are set to random values. As the training process begins, deposit profile values from the training datasets are fed into the input layer. These values propagate through the hidden layers of the DNN, and estimates of the initial flow conditions are outputted at the output layer. At this point in the training process, the DNN model is yet to adapt its internal variables to the functional relationship between turbidite deposits and initial flow conditions. Thus, the initial estimates are expected to largely differ from the actual values. To explore

this functional relationship, a loss function is used to evaluate the accuracy of the estimated values. The loss function used in this case is the mean squared error function, which is considered as one of the best functions for regression (Wang & Bovik, 2009). The gradient of the loss function is calculated and fed back to the hidden layers of the DNN model through backpropagation (Nielsen, 2015; Schmidhuber, 2015), where the internal values of the DNN model are optimized toward minimizing the difference between the estimated and actual values. This process is repeated for every epoch of calculation. An epoch is a cycle of calculation in a DNN that involves one forward pass and one backpropagation of all training data.

The optimization algorithm used in this study is stochastic gradient descent (SGD), which drastically reduces the amount of calculation involved in training without compromising accuracy compared to previous gradient descent algorithms (Bottou, 2010). In this study, Nesterov momentum is used with SGD (Ruder, 2016). Because of the difference in the order of the range of the initial flow conditions, the training datasets should be normalized before they are inputted to the DNN. In this case, all values are normalized to be between 0 and 1 for the DNN model to consider all parameters at equal weights. The hyperparameters, including the number of layers, number of nodes at each layer, dropout rate, validation split, learning rate, batch size, epoch, and momentum, were adjusted manually. Various combinations were attempted. The best combination of hyperparameters was chosen on the basis of the performance of the DNN, which is judged on the basis of the final validation loss.

In this study, the DNN model was developed using Python with the package Keras 2.2.4. The package Tensorflow 1.14.0 (Abadi et al., 2015) was used for backend calculations. Calculations were performed using GPU NVIDIA GeForce GTX 1080 Ti.

3.3 Evaluation of Trained DNN Model

During the verification of the DNN model with test numerical datasets (Section 5.1), the reconstruction result of each parameter was evaluated using bias (B) and sample standard deviation (s) of residuals. The calculations were performed using the following equations:

$$B = \frac{\sum x_i}{n}, \quad (17)$$

$$s = \sqrt{\frac{\sum (x_i - B)^2}{n - 1}}, \quad (18)$$

where n represents the number of test datasets, and x_i denotes the residual of the specific reconstructed parameter for the i th test dataset. The value of s for each reconstructed parameter was compared with a representative value C_v^* , which is the mid-value over the range in which the specific parameter was generated (Table 1). The confidence interval of B was determined using the bootstrap resampling method (Davison & Hinkley, 1997). Resampling of B was conducted 10000 times, and the 95% confidence interval (CI) of B was determined.

During the verification of the DNN model using flume experiment data (Section 5.2), linear interpolation was first applied to the sampled experimental deposit datasets so that the number of data points for one experimental dataset was the same as that for a training dataset. Then, flow parameters at the upstream end of the simulation were reconstructed from the measured properties of the deposit profile. The upstream end of the simulation was set at 1.0 m from the inlet of the flume. The reconstructed parameters were inputted into the forward model so that downstream flow parameters and the time evolution of the deposit profile were calculated. The calculated downstream flow parameters were compared with the flow conditions measured during experiments. The deposit profile calculated from the reconstructed flow

parameters was also compared with the measured deposit profile that was used for inversion.

To evaluate the precision of reconstruction, Jackknife method (McIntosh, 2016) was applied to the sampled deposit values and delete-1 Jackknife samples were generated. Inverse analysis by the DNN model was performed for the delete-1 Jackknife samples, and downstream flow parameters were calculated for each sample. There were 18 delete-1 Jackknife samples for each experiment, since the deposits were sample at 18 locations. Considering the small sample size (less than 30), t-distribution was used instead of normal distribution. The 95% confidence interval of t-distribution is $\pm(t \times s_{\bar{x}})$, where $s_{\bar{x}}$ is the standard error and is defined by the following equations:

$$\bar{x} = \frac{\sum_{i=1}^n x_i}{n}, \quad (19)$$

$$s_{\bar{x}} = \sqrt{\frac{\sum_{i=1}^n (x_i - \bar{x})^2}{n(n-1)}}, \quad (20)$$

where n represents the sample size, x_i denotes the jackknife sample where the i th sampled deposits value were eliminated, and \bar{x} is the mean of x_i . The value t is a standardized value determined by the degree of freedom and the alpha level. Degree of freedom is the sample size subtracted by 1. In this case, the sample size is 18, thus df is 17. For 95% confidence interval, the alpha level is 0.05. According to the two-tails t-distribution table, t for our samples is 2.110.

4 Flume Experiments

4.1 Experiment Settings

The flume was made of acrylic panels and was 4 m in length, 0.12 m in width, and 0.5 m in depth. During the experiments, it was submerged in a tank made of glass panels and a steel supporting frame. The tank was 5.5 m in length, 2.5 m in width, and 1.8 m in depth. The slope of the channel floor changed at 1.0 m from the inlet, where a was the upstream slope and b was the downstream slope (Figure 4). Values of a and b for each experiment are stated in Table 2.

Sediment was mixed with water in two mixing tanks before the experiments. During the experiments, the mixture of sediment and water was first pumped to the constant head tank and then released into the flume. The flow into the flume was controlled via a valve at the base of the constant head tank. Flow discharge was regulated by changing the degree of valve opening. The amount of mixture in the constant head tank was kept at a constant level during the experiments to maintain a stable flow discharge. The damping tank at the downstream end of the flume prevented any reflection of flow toward the upstream direction. A pipe of freshwater supply was placed at the top of the damping tank, and a draining pipe was placed at the bottom of the damping tank. The combination of these two pipes kept the level of water in the tank constant and prevented the reflection of flow.

Five experiments were conducted using plastic particles in this study. The density of the plastic particles used was 1.45 g/cm³. Two experiments (experiments PP1, PP2) were performed using polyvinyl chloride, which had an average grain diameter of 0.120 mm, and melamine, which had an average grain diameter of 0.220 mm (Section 4.3). Three experiments (experiments PP3, PP4, PP5) were performed with two types of melamine, which had an average grain diameter of 0.120 mm and 0.220 mm, respectively (Section 4.3).

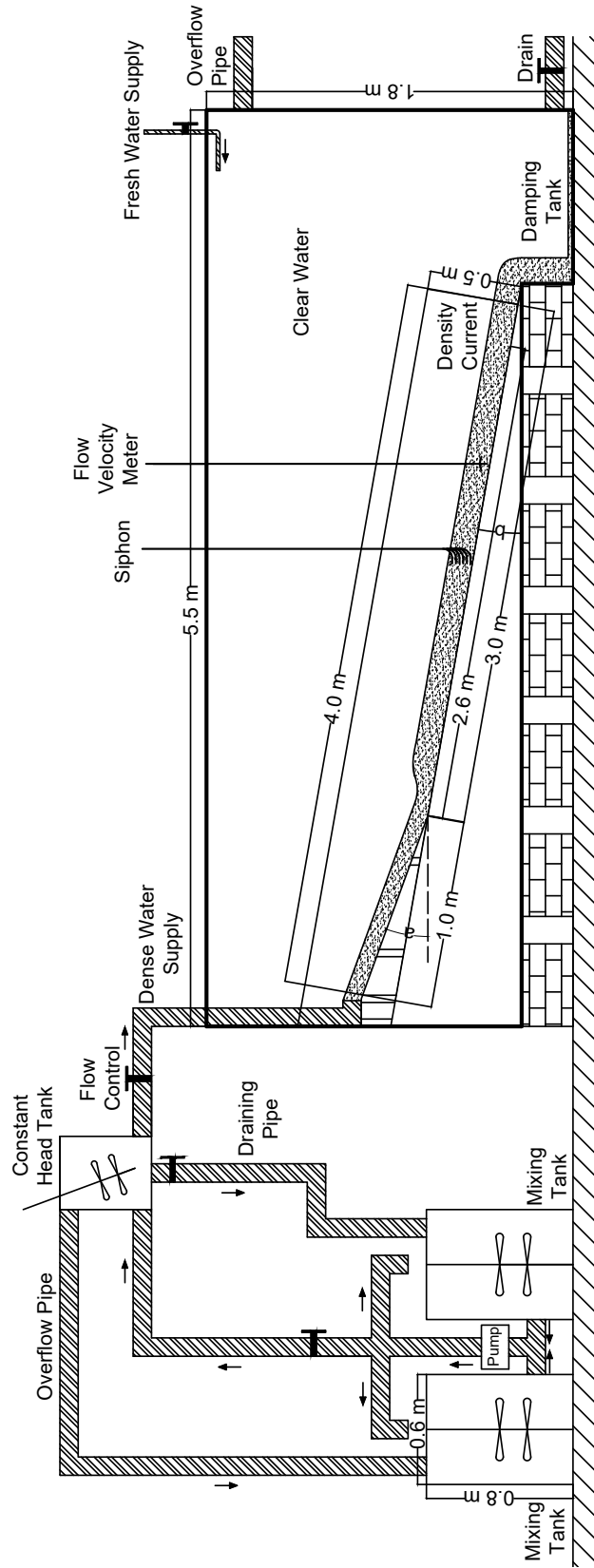


Figure 4. Schematic diagram of flume used for experiment.

4.2 Measurements and Data Analysis

Before each experiment, the tank water temperature was measured using a glass alcohol thermometer. The mixture in the tank was sampled with a 500 mL beaker to measure the initial concentration in the tank. Flow velocity was measured using an acoustic Doppler velocity profiler (ADVP; Nortek Vectrino Profiler). The maximum functional range of the ADVP used was 4.0 – 7.0 cm below the probe. The actual range of reliable measurement may be shorter if the signal-to-noise ratio (SNR) of data collected is below a certain threshold (Appendix A). To obtain the vertical velocity profile of the flow, an actuator was used to adjust the position of the ADVP during the experiments.

A siphon with 10 plastic tubes was used to measure the suspended sediment concentration of the flow. The tubes were aligned vertically at 1.0 cm intervals and were positioned such that samples were collected at 0.0 to 9.0 cm above the bed. Aluminum tubes with an outer diameter of 8.0 mm and an inner diameter of 5.0 mm were attached to the outlets of plastic tubes to keep them in place. Sampling by siphon was conducted when the flow reached a quasi-equilibrium state. The state of flow was determined by observing the development of the flow. Two single-lens reflex cameras were used to record the experiments. Flow depth was determined based on the video recorded.

After the experiments, the flume was left untouched for 1 to 3 days for the suspended sediment to settle. Afterward, photos were taken from a lateral view perpendicular to the flume. The lateral view of the deposited sediment was photographed with a ruler beside it. The height of the deposit was determined from the photos. Water was then gradually drained from the tank with a bath pump at a rate of 0.0002333 m³/s. After the water was drained, deposited sediment was sampled at 20 cm intervals starting from the upstream boundary of the flume.

Samples from the siphon and the mixing tank were first weighed immediately after they were collected. Then, they were dried in a drying oven at 70°C along with the deposit samples. Samples from the siphon and the mixing tank were weighed again after drying. The measurements were used for calculating the sediment concentration in the flow and tank. Grain size distribution analysis was performed in a settling tube for all dried sediment samples. The settling tube used was 1.8 m in length. The calculation of grain size distribution was performed using STube (Naruse, 2005). Particle settling velocity was calculated using Gibbs (1974). The measured grain size distribution of sediment was discretized to four grain-size classes. The representative grain diameter of grain-size classes 1, 2, 3, and 4 were set to be 210, 149, 105, and 74.3 μm , respectively.

In steady flow conditions, the relationship between the layer-averaged flow velocity U , the layer-averaged sediment volumetric concentration C , and the flow depth H is defined as follows (Garcia & Parker, 1993):

$$UCH = \int_a^\infty u_z c_z dz, \quad (21)$$

where u_z and c_z represent the flow velocity and sediment volumetric concentration, respectively, at elevation z above the bed. The relationship between the layer-averaged flow velocity U and the velocity maximum U_m is defined by the following equation (Altinakar et al., 1996):

$$\frac{U_m}{U} = 1.3. \quad (22)$$

The layer-averaged flow velocity was calculated from the velocity maximum of the profile measured by the ADVP using the relationship described by equation 22. The

sediment volumetric concentration was calculated from siphon measurements using the relationship described by equation 21.

4.3 Experimental Conditions

Experimental conditions for the five runs conducted are outlined in Table 2. C_{TT} represents the total concentration of sediment in the mixing tank. C_{1T} , C_{2T} , C_{3T} , and C_{4T} represent the concentrations of grain-size classes 1, 2, 3, and 4, respectively. Parameter x_C represents the position of the siphon downstream, whereas x_U represents the position of ADVP downstream. x_H represents the position in which the flow depth was measured from a video taken during the experiments. x_U , x_C and x_H were changed for each run because of limitations in the flume setup at the time of the experiments. Temperature is the measured temperature of clear water in the tank before the experiments.

Table 2. Conditions and settings of experiments conducted.

	PP1	PP2	PP3	PP4	PP5
C_{TT}	0.0191	0.0276	0.0120	0.0141	0.0101
C_{1T}	0.0102	0.0160	0.00230	0.00453	0.00290
C_{2T}	0.00713	0.00820	0.00670	0.00657	0.00446
C_{3T}	0.00146	0.00254	0.00250	0.00246	0.00199
C_{4T}	0.000366	0.000817	0.000460	0.000567	0.000766
x_C (m)	1.08	2.10	1.50	1.50	1.50
x_U (m)	1.46	2.48	1.20	1.20	1.20
x_H (m)	1.10	1.10	1.20	1.20	1.20
Temperature ($^{\circ}\text{C}$)	22.5	17.0	13.0	13.5	14.0
Slope a	26.8%	26.8%	25.6%	25.6%	25.6%
Slope b	10.0%	10.0%	8.00%	8.00%	8.00%

5 Results

Inverse analysis was applied to deposits within a 2.6 m range downstream of the beginning of slope b (1.0 m from the inlet of flow). Due to the limited size of the flume, slope a was set to a steep angle (26.8% or 25.6%) in all five experiments to ensure that the flow accelerates sufficiently for entrainment to occur. Considering the instabilities near the inlet and the overly steep slope, the region with slope a was excluded from numerical simulations and inverse analysis. For the generation of numerical datasets, the upstream boundary of the simulation was set at the beginning of slope b , and calculations were performed for a 3.0 m range downstream. The actual sampling of experiment deposits was performed only up to 2.6 m from the beginning of slope b (Figure 4), because deposits beyond the region were too thin to be collected for some experiments. Only simulation data from the same range were used for training and verification to match the actual sampling range of experiment deposits.

For hyperparameters used during training, the dropout rate, validation split, and momentum for the DNN model were set to 0.5, 0.2, and 0.9, respectively. The learning rate was set to 0.01. The batch size was set to 32 and the number of layers was set to 5. The number of nodes each layer was 2000. Epoch was 20000. With this setting the validation loss was 0.0033 for training with 10.0% slope datasets and 0.0038 for training with 8.00% slope datasets. Figures 5A and 6A show that overlearning did not

occur, as no deviation was observed between the resulting values of the loss functions for the training and validation datasets.

5.1 Verification of Inverse Model with Test Numerical Datasets

This section presents the verification results with numerical test datasets. Parameter reconstruction results by the DNN model are shown in Figures 5 and 6. Parameters reconstructed include flow duration T_d and flow conditions at the upstream end (flow velocity U_0 , flow depth H_0 , and sediment concentrations $C_{i,0}$). Separate verification was performed with numerical datasets of experiments conducted with 10.0% slope and 8.00% slope. Verification results are described in Sections 5.1.1 and 5.1.2.

5.1.1 Verification with Test Numerical Datasets of Experiments Conducted with 10.0% Slope

Overall, the reconstructed values mostly matched with the original values, with a few outliers (Figure 5B-H). However, a greater degree of scattering was observed for T_d compared with other parameters. T_d seemed show a tendency of being underestimated (Figure 5B). The ranges of misfit ($2s$) were reasonable for all parameters, which had $2s/C_v^*$ values under 22.0% (Table 3). For $C_{i,0}$, zero was within the 95% CI of B , but not for T_d , U_0 , and H_0 . CI range was below zero for T_d and U_0 and above zero for H_0 .

Table 3. Sample standard deviation and bias of the inversion result for numerical datasets of experiments conducted with 10.0% slope.

Parameters	s	C_v^*	$2s/C_v^*$	B	CI of B
U_0 (m/s)	0.00577	0.105	0.110	-0.00234	(-0.00316, -0.00155)
H_0 (m)	0.00978	0.155	0.126	0.00164	(0.000286, 0.00301)
T_d (s)	68.6	630	0.218	-49.4	(-59.1, -40.1)
$C_{1,0}$	0.000254	0.0026	0.195	0.0000318	(-0.00000234, 0.0000679)
$C_{2,0}$	0.000278	0.0026	0.214	0.0000292	(-0.00000832, 0.0000681)
$C_{3,0}$	0.000280	0.0026	0.215	0.0000149	(-0.0000237, 0.0000536)
$C_{4,0}$	0.000271	0.0026	0.209	0.0000234	(-0.0000130, 0.0000617)

5.1.2 Verification with Test Numerical Datasets of Experiments Conducted with 8.00% Slope

Overall, good correlations were observed for the reconstructed and original values of flow parameters. The reconstructed values were mostly consistent with the original values, with a few outliers (Figure 6B-H). Similar to the test datasets described in Section 5.1.1, a tendency of underestimation was observed for T_d (Figure 6B). The range of misfit ($2s$) was reasonable for all parameters, which had $2s/C_v^*$ values under 23.0% (Table 4). Zero was included in the 95% CI of B for U_0 , $C_{2,0}$, and $C_{3,0}$, but not for T_d , H_0 , $C_{1,0}$, and $C_{4,0}$. CI range was below zero for T_d and H_0 and above zero for $C_{1,0}$ and $C_{4,0}$.

5.2 Inverse Analysis of Flume Experiment Data

In this section, the calculated deposit profiles and grain size distributions are compared with the actual deposit profiles sampled from the experiments (Figures 7, 8). The results of the reconstructed flow conditions, including flow velocity U_{x_U} , flow

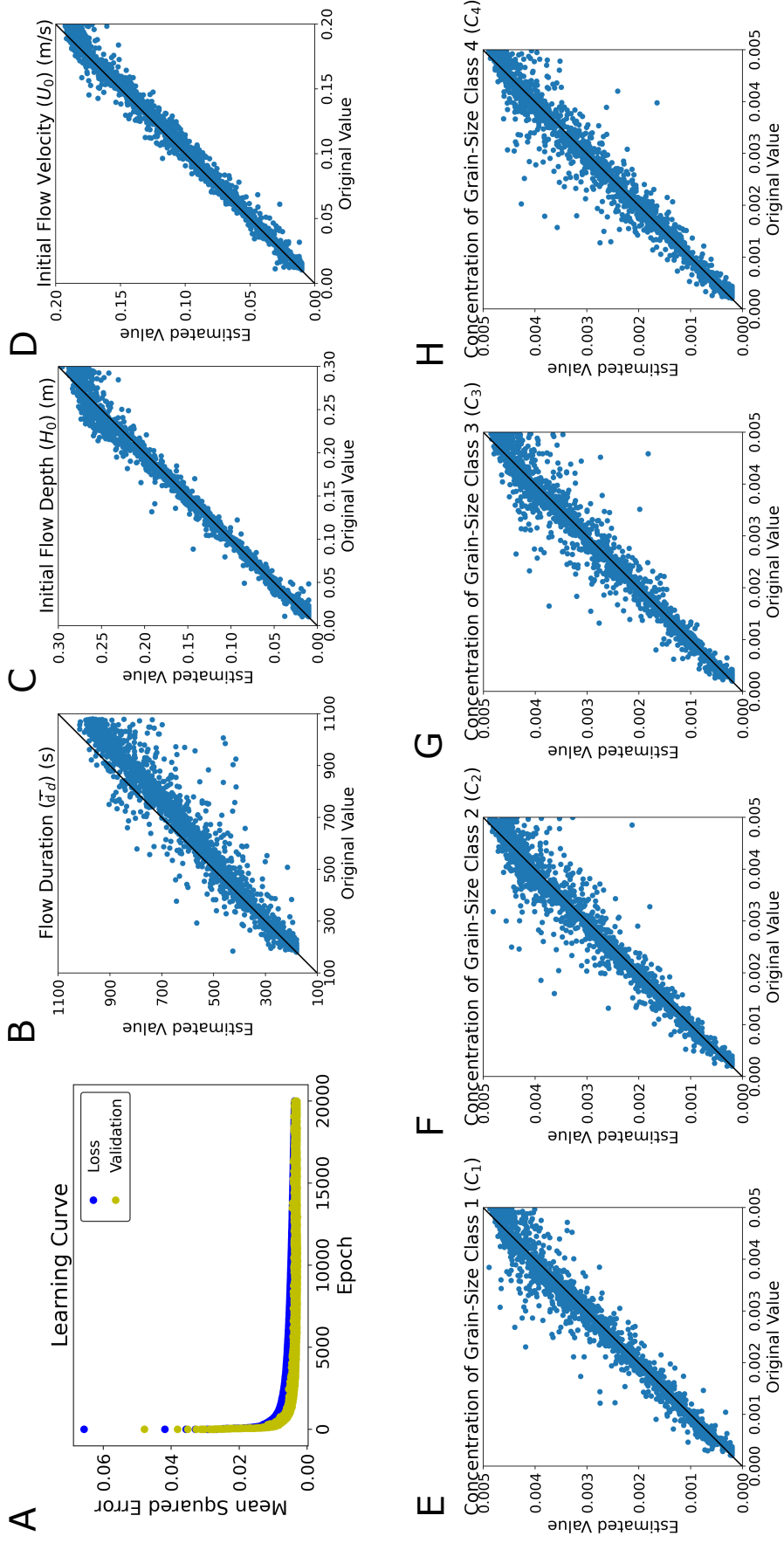


Figure 5. Results of verification with independent numerical datasets (slope = 10.0%). The black diagonal line in each graph is where values on the x -axis (the true values) equal to the values on the y -axis (the estimated values). If a point lies on this line, the reconstructed value matches the true value perfectly. A. Learning curve. B. Estimates of T_d . C. Estimates of H_0 . D. Estimates of U_0 . E. Estimates of $C_{1,0}$. F. Estimates of $C_{2,0}$. G. Estimates of $C_{3,0}$. H. Estimates of $C_{4,0}$.

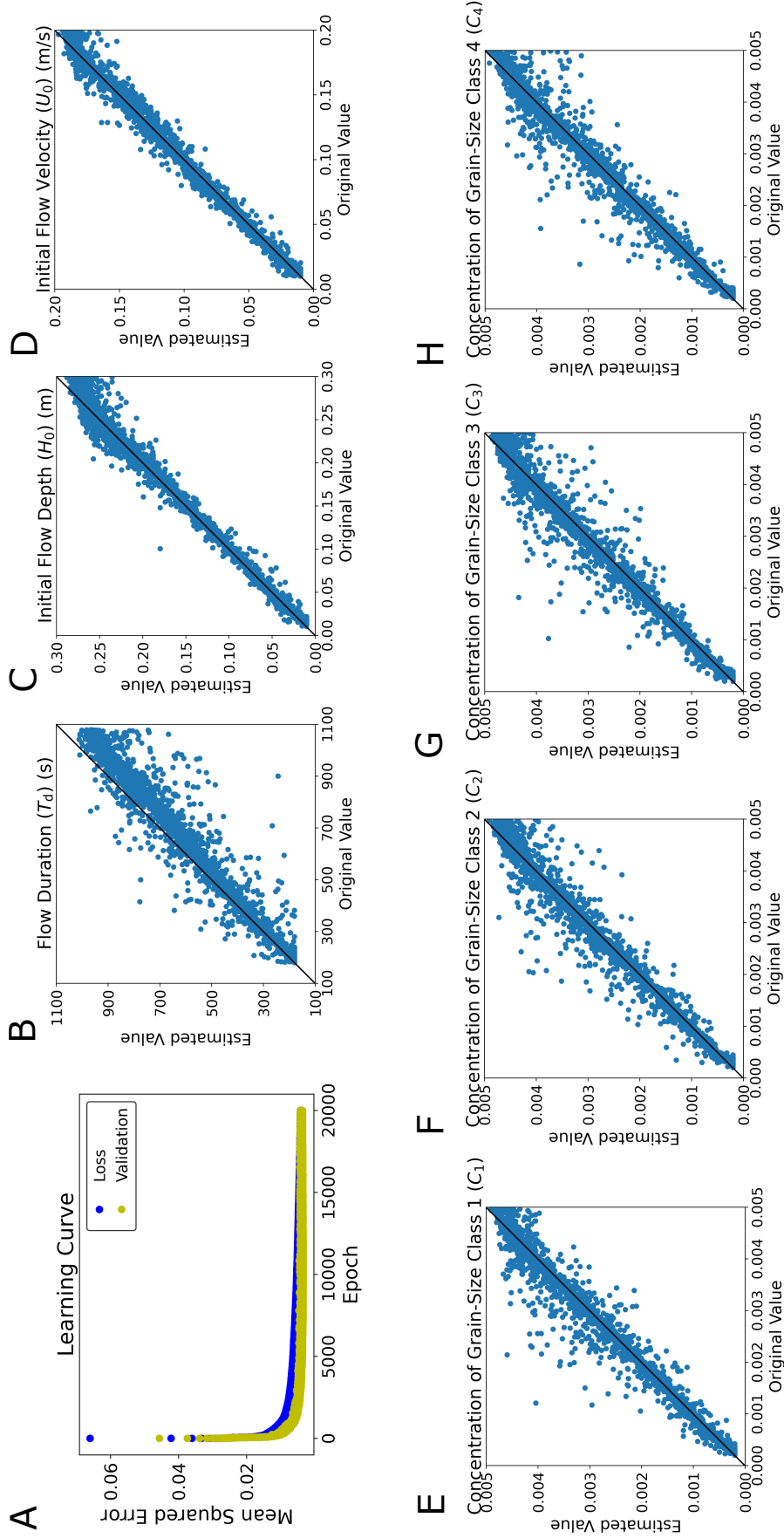


Figure 6. Results of verification with independent numerical datasets (slope = 8.00%). The black diagonal line in each graph is where values on the x -axis (the true values) equal to the values on the y -axis (the estimated values). If a point lies on this line, the reconstructed value matches the true value perfectly. A. Learning curve. B. Estimates of T_d . C. Estimates of H_0 . D. Estimates of U_0 . E. Estimates of $C_{1,0}$. F. Estimates of $C_{2,0}$. G. Estimates of $C_{3,0}$. H. Estimates of $C_{4,0}$.

Table 4. Sample standard deviation and bias of the inversion result for numerical datasets of experiments conducted with 8.00% slope.

Parameters	s	C_v^*	$2s/C_v^*$	B	CI of B
U_0 (m/s)	0.00637	0.105	0.121	0.000369	(-0.000532, 0.00124)
H_0 (m)	0.0107	0.155	0.138	-0.00225	(-0.00376, -0.000790)
T_d (s)	72.1	630	0.229	-47.3	(-57.4, -37.5)
$C_{1,0}$	0.000285	0.0026	0.219	0.0000538	(0.0000149, 0.0000947)
$C_{2,0}$	0.000279	0.0026	0.215	0.0000339	(-0.00000493, 0.0000736)
$C_{3,0}$	0.000296	0.0026	0.228	0.0000393	(-0.00000157, 0.0000806)
$C_{4,0}$	0.000288	0.0026	0.221	0.0000464	(0.00000740, 0.0000871)

depth H_{x_H} , sediment concentrations C_{x_C} , and flow duration T_d , are compared with the measured values (Tables 5 and 6). H_{x_H} is the flow depth H at position x_H (see the positions in Table 2) downstream when the flow reached a quasi-equilibrium state. U_{x_U} is the velocity U at position x_U downstream when the flow reached a quasi-equilibrium state. C_{x_C} is the C at position x_C downstream when the flow reached a quasi-equilibrium state. Inverse analysis results of the experiments conducted with 10.0% slope (PP1, PP2) and 8.00% slope (PP3, PP4, PP5) are described in Sections 5.2.1 and 5.2.2.

5.2.1 Experiments Conducted with 10.0% Slope (PP1, PP2)

Deposit profiles of experiments PP1 and PP2 demonstrated a thinning and fining downstream trend with concave-upward geometry. For both runs, the reconstructed deposit profiles of the total deposition almost entirely overlapped with the sampled data (Figures 7A(1), B(1)). The reconstructed grain size distributions at 1.4 m and 1.8 m downstream also agreed well with the measured values for both experiments (Figures 7A(2),(3), B(2),(3)).

For flow depth H_{x_H} , the measured and reconstructed values were in good agreement (Figure 9A). The measured H_{x_H} of PP1 was 0.116 m and the reconstructed value was 0.157 m with a uncertainty range (95% confidence interval) of ± 0.00921 m. The measured H_{x_H} of PP2 was 0.123 m and the reconstructed value was 0.142 m with a uncertainty range of ± 0.00849 m. Reconstructed H_{x_H} of both PP1 and PP2 had a relatively small uncertainty range in comparison to the measured and reconstructed values. The percent errors between reconstructed and measured H_{x_H} were 35.1% and 15.3% for PP1 and PP2, respectively (Table 5). For flow velocity U_{x_U} , the measured value of PP1 was 0.0812 m/s and the reconstructed value was 0.793 m/s with a uncertainty range of ± 0.00360 m/s. The measured U_{x_U} of PP2 was 0.924 m/s and the reconstructed value was 0.109 m/s with a uncertainty range of ± 0.00817 m/s. The uncertainty range of reconstructed U_{x_U} for both PP1 and PP2 were also relatively small in comparison to the measured and reconstructed values. The percent errors between reconstructed and measured U_{x_U} were 2.38% and 17.9%, of which that of PP1 was lower than that of PP2.

The measured value of flow duration T_d for PP1 was 936 s and the reconstructed value was 494 s with a uncertainty range of ± 58.6 s. The measured T_d for PP2 was 966 s and the reconstructed value was 920 s with a uncertainty range of ± 72.6 s. The percent errors between reconstructed and measured T_d were 47.2% (PP1) and 4.76% (PP2). Reconstructed values for T_d were lower than the measured values (Table 5). The measured value of total flow concentration C_{T,x_C} for PP1 was 0.000808 and the

reconstructed value was 0.00702 with a uncertainty range of ± 0.000667 . The measured C_{T,x_C} for PP2 was 0.00410 and the reconstructed value was 0.00344 with a uncertainty range of ± 0.000462 . The percent errors between reconstructed and measured C_{T,x_C} were 768% (PP1) and 16.1% (PP2), of which that of PP1 had a significantly larger deviation than that of PP2. The reconstructed values of each grain-size class were mostly overestimated (Figure 9D).

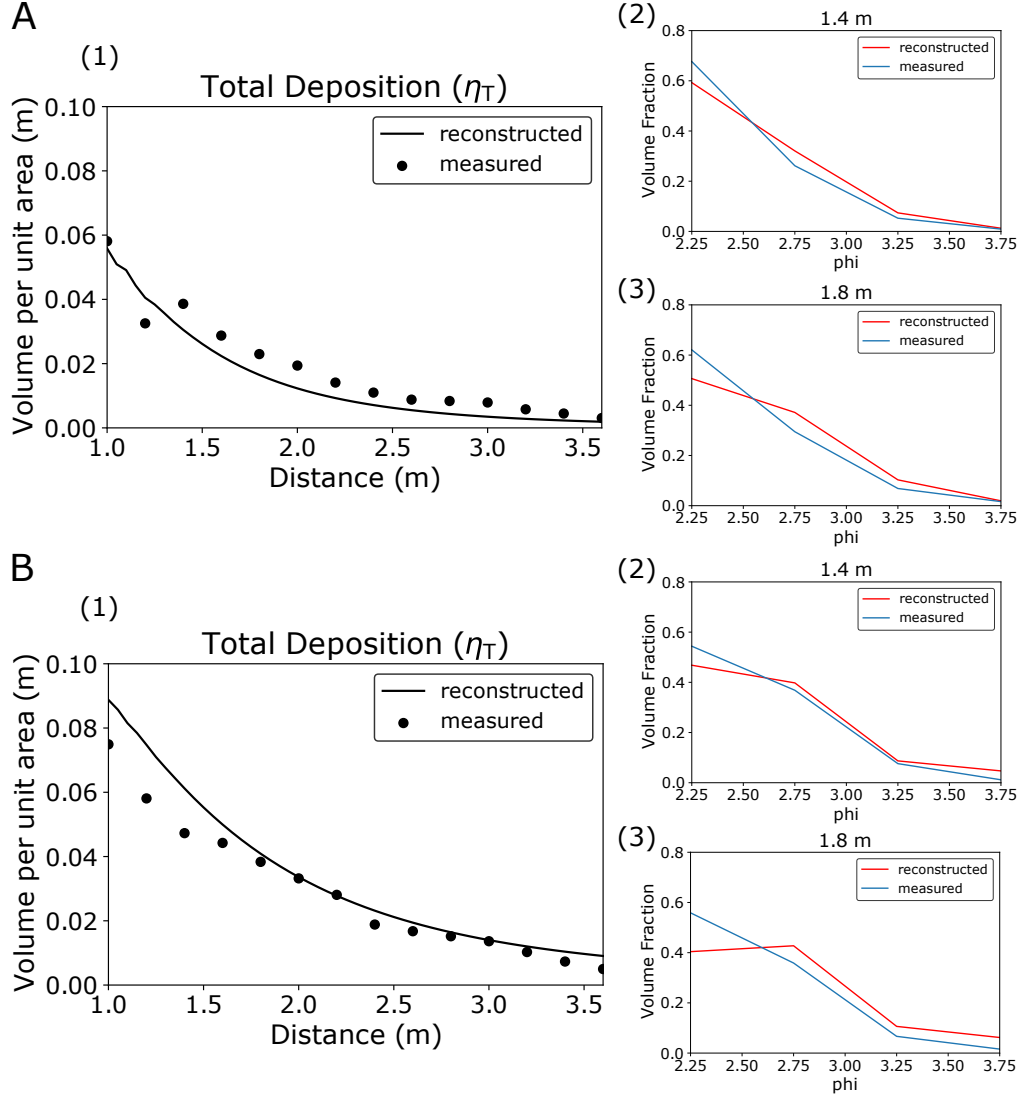


Figure 7. Reconstructed deposit profiles and sampled deposit data of experiments PP1 and PP2. A. (1) Reconstructed and sampled η_T of PP1. (2) Grain size distribution at 1.4 m downstream. (3) Grain size distribution at 1.8 m downstream. B. (1) Reconstructed and sampled η_T of PP2. (2) Grain size distribution at 1.4 m downstream. (3) Grain size distribution at 1.8 m downstream.

5.2.2 Experiments Conducted with 8.00% Slope (PP3, PP4, PP5)

Similar to the results of PP1 and PP2, deposit profiles in experiments PP3, PP4, and PP5 showed thinning and fining downstream trends. The reconstructed

Table 5. Measured and reconstructed flow conditions for experiments PP1 and PP2. (R.: Reconstructed, M.: Measured)

Parameters	PP1		PP1		PP2		PP2	
	R.	M.	Percent Error	R.	M.	Percent Error		
C_{T,x_C}	0.00702 ± 0.000667	0.000808	768%	0.00344 ± 0.000462	0.00410	16.1%		
C_{1,x_C}	0.00333 ± 0.000274	0.0000911	3560%	0.000623 ± 0.0000924	0.000612	1.80%		
C_{2,x_C}	0.00250 ± 0.000244	0.000389	541%	0.00135 ± 0.000189	0.00224	39.9%		
C_{3,x_C}	0.000915 ± 0.000125	0.000228	302%	0.000683 ± 0.0000834	0.000944	27.7%		
C_{4,x_C}	0.000272 ± 0.0000509	0.0000999	172%	0.000788 ± 0.000106	0.000303	160%		
H_{x_H} (m)	0.157 ± 0.00921	0.116	35.1%	0.142 ± 0.00849	0.123	15.3%		
U_{x_U} (m/s)	0.0793 ± 0.00360	0.0812	2.38%	0.109 ± 0.00817	0.0924	17.9%		
T_d (s)	494 ± 58.6	936	47.2%	920 ± 72.6	966	4.76%		

deposit profiles of the total deposition closely matched the sampled data for PP4 and PP5 (Figures 8B(1), C(1)) but was slightly greater than the measured values for PP3 (Figure 8A(1)). The reconstructed grain size distributions at 1.4 m and 1.8 m downstream agreed well with the measured values for all three experiments (Figures 8A(2),(3), B(2),(3), C(2),(3)).

The measured H_{x_H} of PP3 was 0.149 m and the reconstructed value was 0.192 m with a uncertainty range (95% confidence interval) of ± 0.0145 m. The measured H_{x_H} of PP4 was 0.232 m and the reconstructed value was 0.258 m with a uncertainty range of ± 0.0180 m. For PP5, the measured H_{x_H} was 0.196 m and the reconstructed value was 0.126 m with a uncertainty range of ± 0.00925 m. Reconstructed H_{x_H} of PP3, PP4, and PP5 had a relatively small uncertainty range in comparison to the measured and reconstructed values. The percent errors between reconstructed and measured H_{x_H} were 28.8%, 11.1%, and 35.7% for PP3, PP4 and PP5, respectively (Table 6). Of these values, that of PP5 was slightly higher than those of PP3 and PP4. The measured U_{x_U} of PP3 was 0.113 m/s and the reconstructed value was 0.150 m/s with a uncertainty range of ± 0.00508 m/s. The measured U_{x_U} of PP4 was 0.109 m/s and the reconstructed value was 0.172 m/s with a uncertainty range of ± 0.00147 m/s. For PP5, the measured U_{x_U} was 0.137 m/s and the reconstructed value was 0.183 m/s with a uncertainty range of ± 0.00451 m/s. Reconstructed U_{x_U} of PP3, PP4 and PP5 had a relatively small uncertainty range in comparison to the measured and reconstructed values. The percent errors between reconstructed and measured U_{x_U} were 33.2% (PP3), 57.6% (PP4), and 73.7% (PP5), in which PP5 also exhibited a deviation higher than those of PP3 and PP4 (Figure 9B).

The measured T_d of PP3 was 740 s and the reconstructed value was 689 s with a uncertainty range of ± 82.5 s. The measured T_d of PP4 was 332 s and the reconstructed value was 974 s with a uncertainty range of ± 46.8 s. For PP5, the measured T_d was 408 s and the reconstructed value was 264 s with a uncertainty range of ± 17.4 s. The percent errors between reconstructed and measured T_d were 7.16% (PP3), 193% (PP4), and 35.3% (PP5), of which PP4 showed a much larger deviation than PP3 and PP5. The measured C_{T,x_C} of PP3 was 0.00227 and the reconstructed value was 0.00580 with a uncertainty range of ± 0.000443 . The measured C_{T,x_C} of PP4 was 0.00533 and the reconstructed value was 0.00151 with a uncertainty range of ± 0.000385 . For PP5, the measured C_{T,x_C} was 0.00331 and the reconstructed value was 0.00564 with a uncertainty range of ± 0.000342 . The percent errors between reconstructed and measured C_{T,x_C} were 155% (PP3), 71.7% (PP4), and 70.1% (PP5), where PP3 showed a greater deviation than the other two experiments. The concentrations of individual grain-size classes were mostly overestimated (Figure 9D).

6 Discussion

6.1 Validation of DNN as an Inversion Method for Turbidity Currents Using Numerical Test Datasets

Verification results using numerical datasets proved the ability of the DNN model to reasonably reconstruct the hydraulic conditions of turbidity currents from turbidites. Reconstructions of initial flow conditions and the flow duration using numerical datasets (Sections 5.1.1 and 5.1.2) were good judging from the s and B values (Tables 3 and 4). The reconstructions of the flow duration T_d , flow depth H_0 , velocity U_0 , and sediment concentrations $C_{1,0}$, $C_{2,0}$, $C_{3,0}$, and $C_{4,0}$ showed high (Tables 3 and 4).

Correlations between the actual and reconstructed values were observed for all parameters. Some outliers were observed for the reconstructed parameters, but most of the reconstructed values were close to the perfect reconstruction line. The range of

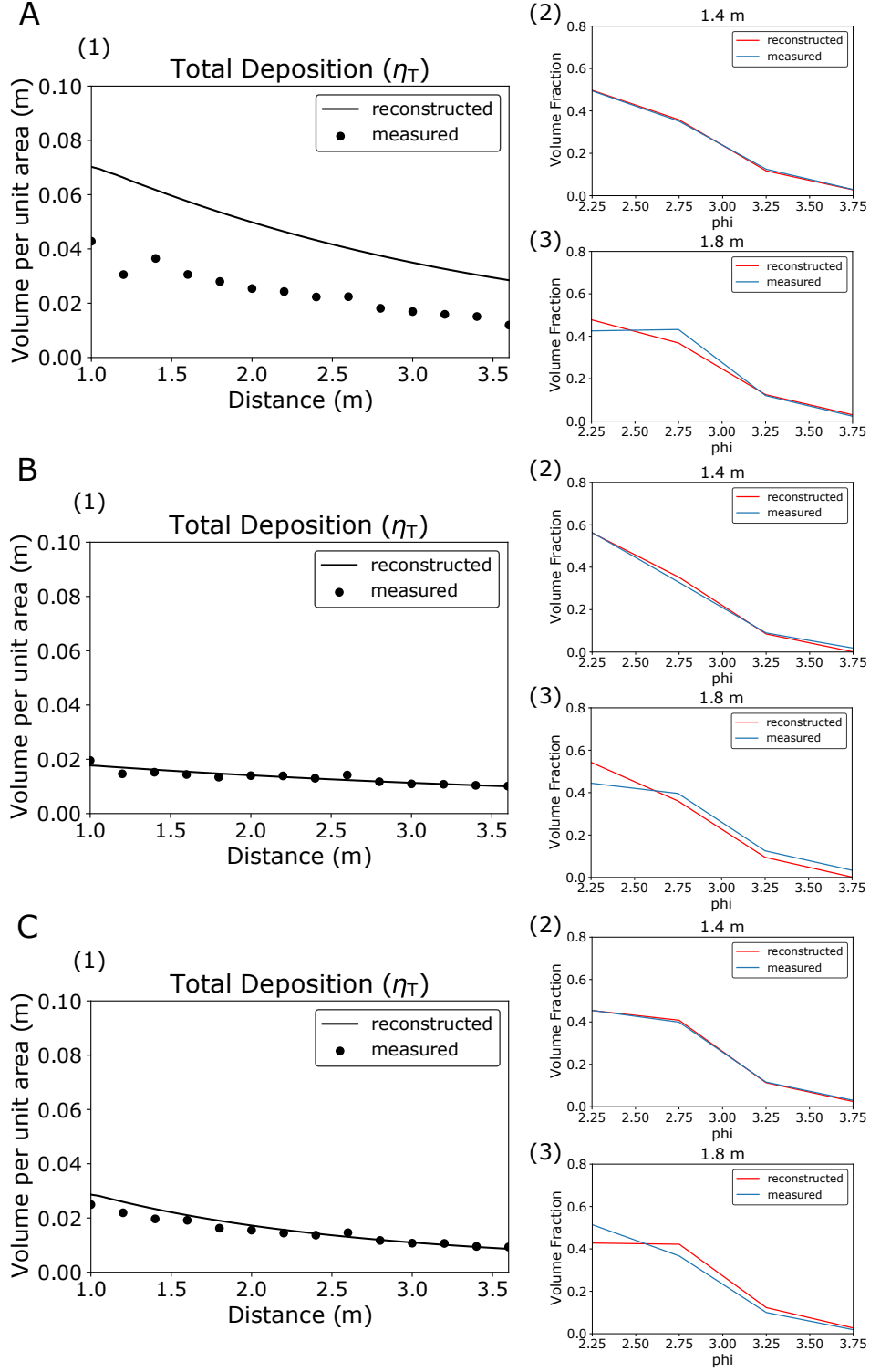


Figure 8. Reconstructed deposit profiles and the sampled deposit data of experiments PP3, PP4 and PP5. A. (1) Reconstructed and sampled η_T of PP3. (2) Grain size distribution at 1.4 m downstream. (3) Grain size distribution at 1.8 m downstream. B. (1) Reconstructed and sampled η_T of PP4. (2) Grain size distribution at 1.4 m downstream. (3) Grain size distribution at 1.8 m downstream. C. (1) Reconstructed and sampled η_T of PP5. (2) Grain size distribution at 1.4 m downstream. (3) Grain size distribution at 1.8 m downstream.

Parameters	PP3 R.	PP3 M.	Percent Error	PP4 R.	PP4 M.	Percent Error	PP5 R.	PP5 M.	Percent Error
$C_{T,xC}$	0.00580 ± 0.000443	0.00227	155%	0.00151 ± 0.000385	0.00533	71.7%	0.00564 ± 0.000342	0.00331	70.1%
$C_{1,xC}$	0.00142 ± 0.000120	0.000108	1210%	0.000379 ± 0.000106	0.000884	57.1%	0.00108 ± 0.0000556	0.000258	321%
$C_{2,xC}$	0.00218 ± 0.000167	0.00136	59.9%	0.000534 ± 0.000126	0.00313	82.9%	0.00227 ± 0.000116	0.00210	7.80%
$C_{3,xC}$	0.00149 ± 0.000104	0.000646	1310%	0.000420 ± 0.0000814	0.00109	61.5%	0.00149 ± 0.000124	0.000793	88.1%
$C_{4,xC}$	0.000713 ± 0.000105	0.000157	3540%	0.000175 ± 0.0000716	0.000227	22.9%	0.000793 ± 0.0000685	0.000159	3980%
H_{xH} (m)	0.192 ± 0.0145	0.149	28.8%	0.258 ± 0.0180	0.232	11.1%	0.126 ± 0.00925	0.196	35.7%
U_{xU} (m/s)	0.150 ± 0.00508	0.113	33.2%	0.172 ± 0.00147	0.109	57.6%	0.183 ± 0.00451	0.137	73.7%
T_d (s)	687 ± 82.5	740	7.16%	974 ± 46.8	332	193%	264 ± 17.4	408	35.3%

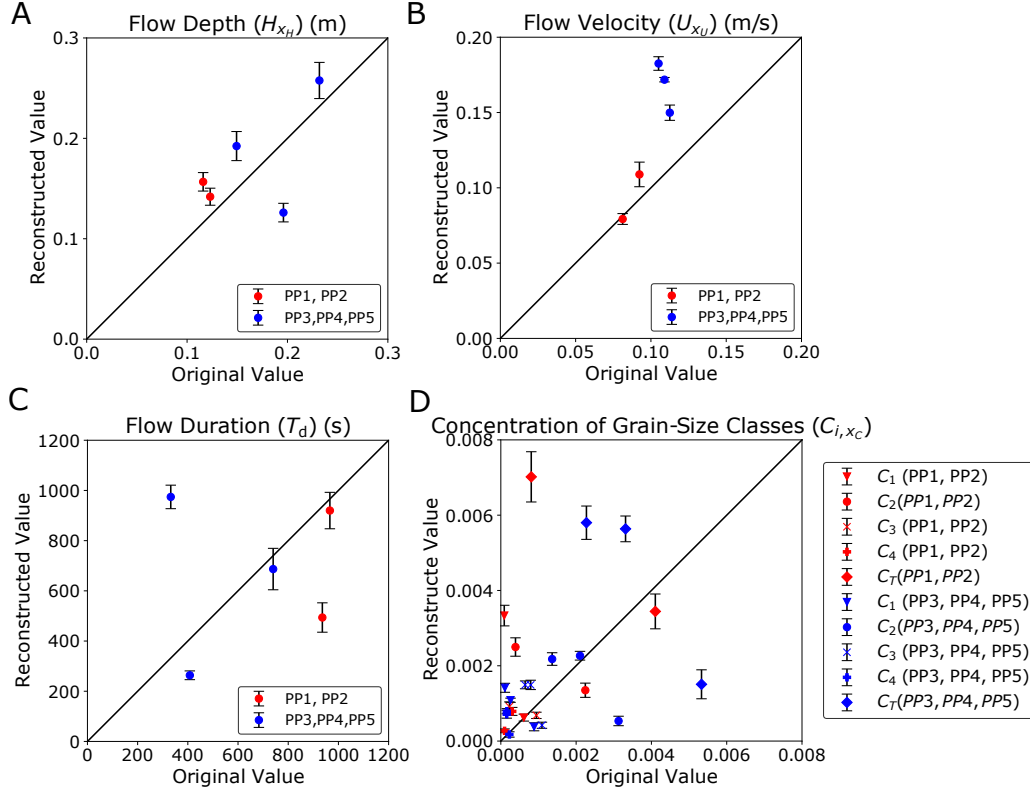


Figure 9. Reconstructed (with 95% confidence interval uncertainty range) vs measured flow conditions for experiments PP1, PP2, PP3, PP4 and PP5. A. Plot for H_{x_H} . B. Plot for U_{x_U} . C. Plot for T_d . D. Plot for C_{i,x_C} .

misfit ($2s$) of all parameters was below 23.0% of the matching representative value (Tables 3 and 4). A relatively greater degree of scattering was observed for T_d compared to the other parameters (Figures 5B and 6B).

Concerning the estimation bias, zero was included in the 95% CI of bias for most of the parameters, proving that the reconstructed values were not significantly biased with respect to the original values. Even among parameters where statistically significant biases were detected, their deviations were minor compared with the representative values of the parameters (Tables 3 and 4). For example, in both numerical datasets of experiments conducted with 10.0% slope and 8.00% slope, the estimation bias B for T_d had a negative value and the range of the CI of B was below zero (Tables 3 and 4), indicating a tendency of underestimation for T_d . However, the bias for T_d was only 7.84% (10.0% slope numerical datasets) or 7.51% (8.00% slope numerical datasets) of the representative value of this parameter (630 s).

Thus, this method is suitable for estimating the paleo-hydraulic conditions of actual experimental scale turbidity currents. Correlation between reconstructed parameters and original values did not show any significant bias, implying that the inverse model developed in this study served as a high precision, high accuracy estimator of flow conditions.

6.2 Verification of DNN Inversion with Flume Experiment Data

As a result of inversion using the DNN model, the overall deposit profiles were reasonably reconstructed for all five experiments, and the reconstructed grain size distribution downstream matched the sampled values from experiment deposits (Figures 7 and 8). The DNN model as an inverse method tries to find the combination of hydraulic conditions that best produces the inputted deposit profiles. The fact that the reconstructed hydraulic conditions reproduced the deposit profiles used for inverse analysis indicated the DNN inverse model performed well.

For the hydraulic conditions and flow duration, a good match was observed for H_{xH} for all five experiments with a percent error under 36.0% (Tables 5 and 6). Flow duration T_d was reasonably reconstructed for PP1, PP2, PP3, and PP5, with a percent error lower than 48.0%. Reconstructed T_d of PP4 had a percent error greater than 190%. The reconstructed concentrations of each grain-size class C_{i,x_C} were mostly overestimated (Figure 9). The measured and reconstructed values of flow velocities U_{xU} agreed well, especially for PP1 and PP2, with a percent error less than 18.0%. U_{xU} reconstructed for PP3, PP4, and PP5 ranged from 33.2% to 73.7%.

The ability of the DNN model to distinguish minor differences in the characteristics of deposits was proved in the tests using numerical datasets, where a wide variety of initial conditions of flows were well reconstructed (Section 5.1). The fact that the DNN model was able to reconstruct the initial flow condition for the artificial test datasets proved that non-uniqueness of deposit was not a problem for the range of flow conditions tested in this study. According to the analysis of the results of the application of the DNN model to flume experiment data, there are three sources of deviations in the reconstruction of hydraulic conditions: (1) measurement errors during and after the experiments, (2) bias inherent in the inverse model, and (3) inaccuracy within the forward model of turbidity currents.

(1) The main source of deviation for sediment concentrations C_{i,x_C} may be inaccuracies in measurements. As shown in Figure 9, some of the measured concentrations C_{i,x_C} were extremely small ($< 0.1\%$), making them susceptible to minor disturbances during sampling and measurements. For extremely small values, even minor deviations appear to be large. Thus, for C_{i,x_C} , the main source of deviation may not be the reconstructed values but the measured values.

As for flow velocity U_{xU} , the accuracy of measurement was greatly affected by the SNR during the experiments. Experiments PP3, PP4, and PP5 had relatively lower SNRs and a narrower range of reliable measurement than PP1 and PP2, with PP4 and PP5 having the lowest SNR (Appendix A). The narrower range of reliable measurement for PP3, PP4, and PP5 resulted in ranges of vertical velocity profile without measurements. The measured values closest to the velocity maximum was used for calculation for PP3, PP4, and PP5, which could be slightly smaller than the actual value. In which case, the calculated layer-averaged flow velocity would also be smaller than the actual value. This may be the reason that U_{xU} of experiments PP3, PP4 and PP5 were overestimated and showed larger deviation than PP1 and PP2.

Slight deviation in the sampling and measurement of the deposits could also be a source of deviation in the eventual reconstruction. The uncertainty range for the reconstructed parameters was calculated using Jackknife samples of the η values measured from the experiment deposits. The width of the uncertainty range showed that slight deviation of the input η values can propagate to the output reconstructed values of H_{xU} , U_{xU} , $C_{i,xC}$, and T_d .

(2) Regarding the inherent bias in the inverse model, the reconstructed T_d for the experiments PP1, PP2, PP3, and PP5 exhibited the same tendencies of deviation during the reconstruction using numerical test datasets. Thus, deviation in the reconstruction of T_d may be partially due to systematic error originating from the internal settings of the DNN.

(3) Inaccuracy in the forward model in describing the physical processes of turbidity currents may account for deviations of the reconstructed flow velocities from the measured values. There are several possible reasons why the reconstruction of flow velocity was not as accurate as with the other parameters, but the most probable reason is the inaccuracy of the entrainment function in describing the actual effect of entrainment in flow, considering that the exponent in the calculation of the dimensionless vertical velocity in the entrainment function was determined purely via optimization and differed greatly in previous studies (Parker et al., 1987; Garcia & Parker, 1991; Dorrell et al., 2018). Another problem may lie in the layer averaging of flow velocity. Dorrell et al. (2014) had pointed out that vertical stratification of flow velocity and density fields reduces depth averaged hydrostatic pressure and enhances suspended sediment and momentum flux, proving that incorporating the effect of flow stratification can be essential for calculating turbidity currents. This research aims to verify the DNN model as a method of inverse analysis of turbidity currents. The improvement of the forward model, including entrainment function and velocity calculation, should be the next step in the inverse analysis study of turbidity currents.

A limitation of the inverse analysis is that it can only be conducted for flow that is depositional. Inverse analysis reconstructs the flow conditions from turbidite deposited by turbidity current, so the model would be unable to detect a non-depositional condition if it happened during a flow. Although unlikely in the current lab setting, there is a possibility that flow parameters cannot be reconstructed when different combinations of initial conditions produce the same deposit profile, which will be a problem to be resolved in the future when using field data. Compared to the analytical models, the shallow water model implemented provides some details of the internal structure of the flow, but also holds certain limitations due to its simplified calculation of flow dynamics. Nonetheless, the simplifications enable large batches of natural scale simulations to be performed. Overall, even though a certain amount of deviation was observed for all parameters, they mostly lie within a reasonable range and provided valuable insights into the development of flow and deposits over time.

6.3 Comparison of DNN with Existing Methodologies

Compared to previous methods of inverse analysis of turbidity currents, the inversion method using the DNN model has great advantages in terms of calculation cost and reconstruction accuracy. Previous inversion methods of turbidity currents seek to optimize flow initial conditions to a particular set of data collected from turbidites, which is extremely time-consuming for application to one dataset and does not guarantee the general applicability of the methods to turbidite deposits (Lesshafft et al., 2011; Parkinson et al., 2017; Nakao et al., 2020). For example, a genetic algorithm used in Nakao et al. (2020) first initializes a population of parameters and then optimizes the population of parameters through selection and mutation. Eventually, the remaining parameters can successfully reconstruct target turbidite. However, each epoch of optimization requires the selection results from the previous epoch, and thus, the calculation of the forward model cannot be parallelized over epochs. In the adjoint method used by Parkinson et al. (2017), control variables within the forward model of turbidity currents are first initialized and inputted into the numerical model. The turbidite deposit profile is calculated and compared with the target values using a cost function. Gradients of the cost function (objective function) for control variables are calculated analytically. If the result is not optimal, the adjoint model will run, and control variables will be adjusted by descent method. The adjusted control variables will be re-inputted into the numerical model. This cycle is repeated until the reconstructed deposit profile is judged to be optimal. Thus, the iteration of calculation cannot be performed simultaneously. In contrast, the DNN model explores the general functional relationship between turbidite deposited and flow, allowing its applicability to turbidity currents in general. The forward model calculation to generate training datasets can be perfectly parallelized, thereby significantly reducing the amount of calculation time.

Since the parallelization of the forward model calculation significantly reduced the calculation time, a more accurate and realistic forward model with a heavier calculation load could be implemented. As a result, the forward model used in this research is much better at capturing the spatio-temporal evolution of turbidity current than the forward model used in previous research (Falcini et al., 2009; Parkinson et al., 2017). Falcini et al. (2009) used a steady flow forward model, whereas our forward model is a non-steady flow model that reproduces the evolution of flow over time. The method implemented in Parkinson et al. (2017) omitted the effect of entrainment, which is a significant part of sediment transport in turbidity currents. As a result, their reconstructed values of flow depth, concentration, and grain diameter of the turbidite were 2.56 km, 0.0494%, and 103 μm , respectively (Parkinson et al., 2017). Compared to the objective values collected from the turbidite deposits, these values showed great deviations. In contrast, our predictions closely agreed with the original values and the effect of sediment suspension was incorporated in our forward model. Another improvement from previous research is that the forward model used in this study applies to turbidite datasets of multiple grain-size classes.

Lesshafft et al. (2011) proposed a method based on direct numerical simulation (DNS) of the Navier-Stokes equations. However, the calculation costs of the method were extremely high, making it impractical to apply the method to natural scale turbidites. The computational cost of DNS was scaled to Re^3 , thereby limiting the effectiveness of DNS to only experimental scale flows (Biegert et al., 2017). As a result, the maximum value of Reynolds number attained in previous numerical simulation using DNS was 15,000 (Cantero et al., 2007), which corresponds to 3.0 cm/s for flow velocity and 50 cm for the flow depth. Thus, their methodology cannot be applied to natural scale turbidites.

7 Conclusions

In this study, a new method for the inverse analysis of turbidites using a DNN model was verified with actual flume experiment data. Compared to previous methods, the DNN model proved to be an efficient method for the inverse analysis of turbidity currents without compromising reconstruction accuracy. The DNN model performed well for verification using numerical datasets, judging by the standard deviation and bias of the reconstructed parameters. In terms of the application of the DNN model to experiment data, deposit profiles were well reconstructed; however, the initial flow conditions did not match the measured values perfectly. The uncertainty range of 95% confidence interval was determined for the reconstructed values of the experiment datasets using Jackknife resampling method.

The reconstructed and measured flow depths H had percent error that is less than 36.0%, which is low for the inverse analysis results. The inverse analysis result for T_d had a percent error ranging from 4.76% to 35.2%, except for PP4, which had a percent error of 193%. U was well reconstructed for experiments PP1 and PP2 (percent error 2.38% and 17.9%) and showed greater deviation for PP3, PP4, and PP5 (percent error 33.2%-73.7%). The reconstructed values for C_i had percent errors ranging from 1.79% to greater than 300%.

Overall, the DNN model exhibited good performance for the inversion of numerical datasets and some parameters of the experiment data. The deposit profiles were well reconstructed, demonstrating the success of the DNN model in exploring the functional relationship between the initial conditions of flow and resulting deposits. The verification results with numerical datasets and flume experiments reveal that the implemented forward model is competent in performing inverse analysis on turbidity currents, but it needs to be more robust for application to a wide range of flow conditions. Improvement of the forward models and parameters, such as the entrainment function, will be a top priority in the future. The DNN's hyperparameter settings and internal structure also have room for improvement, judging from the inversion result using numerical datasets. The application of the DNN model to field datasets will be the eventual goal.

Appendix A Flow Velocity Profile and the Corresponding Signal-to-Noise Ratio (SNR)

The accuracy of flow velocity measurements by the ADV used (Nortek Vectrino Profiler) was affected by the Signal-to-Noise Ratio (SNR). According to the user manual of Nortek Vectrino Profiler, the "weak spot" of acoustic profile measurement due to pulse interference can be detected from the SNR values. The manual states that the SNR value of measurements need to be at least 30 dB to be considered reliable. Data with SNR between 20 dB and 30 dB should be used with caution and data with SNR lower than 20 dB should not be trusted. The measured velocity profile for each experiment and the matching SNR profile are shown in Figures A1 and A2. The height above bed of ADV differed for the experiments conducted, thus the range of measured profiles above bed were also different.

From figures A1 and A2, it was apparent that SNR of velocity measurements for experiments PP1 and PP2 were much higher than those of experiments PP3, PP4, and PP5. The SNR values of PP1 and PP2 were above 40 dB. Experiment PP3 had slightly better SNR profile than PP4 and PP5, with the peak SNR above 40 dB, but the lowest SNR barely above 30 dB. Experiment PP4 had especially low SNR, with the peak SNR slightly above 30 dB. SNR of PP5 was above 40 dB toward the bottom, but decreased below 30 dB toward the top. While the entire velocity profile can be

782 used for analysis of PP1 and PP2, only regions with high SNR can be used for PP3,
 783 PP4, and PP5.

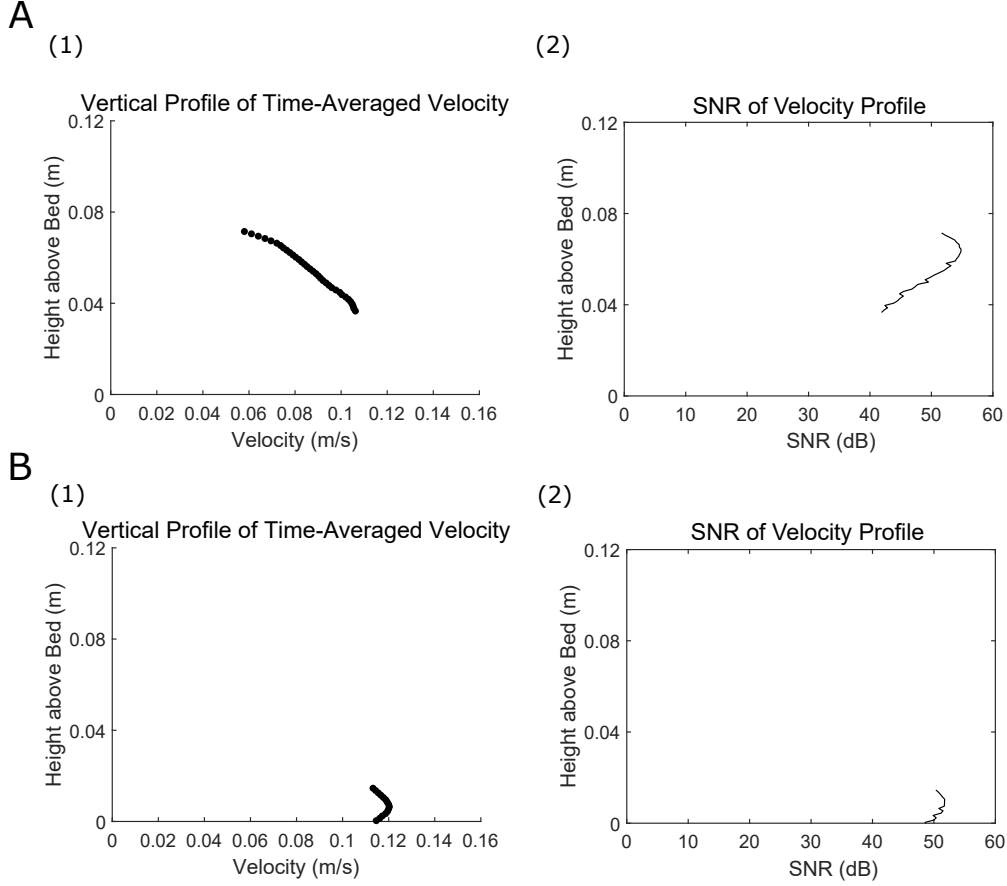


Figure A1. Time-averaged velocity profile and SNR of velocity profile for experiments conducted with 10.0% slope. A. (1) Time-averaged velocity profile of PP1. (2) SNR of velocity profile for PP1. B. (1) Time-averaged velocity profile of PP2. (2) SNR of velocity profile for PP2.

Appendix B Details of Forward Model Implemented

B1 Example of Forward Model Calculation

The forward model was tested with two sets of numerical simulations of turbidity currents. Testing was conducted using the forward model programmed for generating numerical datasets for experiments conducted with a 10% slope. The settings of the numerical simulations are listed in Table B1, whereas the time evolution of the high $C_{T,0}$, U_0 simulation is shown in Figure B1, and the time evolution of the low $C_{T,0}$, U_0 simulation is shown in Figure B2. In both cases, the flow depth H was greater toward the head of the current. H at the head of the current also increased over time (Figures B1A and B2A). Flow velocity U in the high $C_{T,0}$, U_0 simulation increased toward the head of the current (Figure B1B), whereas U in the low $C_{T,0}$, U_0 simulation increased initially, and then decreased toward the head of the current (Figure B2B). The total volumetric concentration of sediment C_T in flow decreased downstream in both cases (Figures B1C and B2C). In the high $C_{T,0}$, U_0 case, a larger portion of sediment was deposited downstream than in the low $C_{T,0}$, U_0 case (Figures B1D and

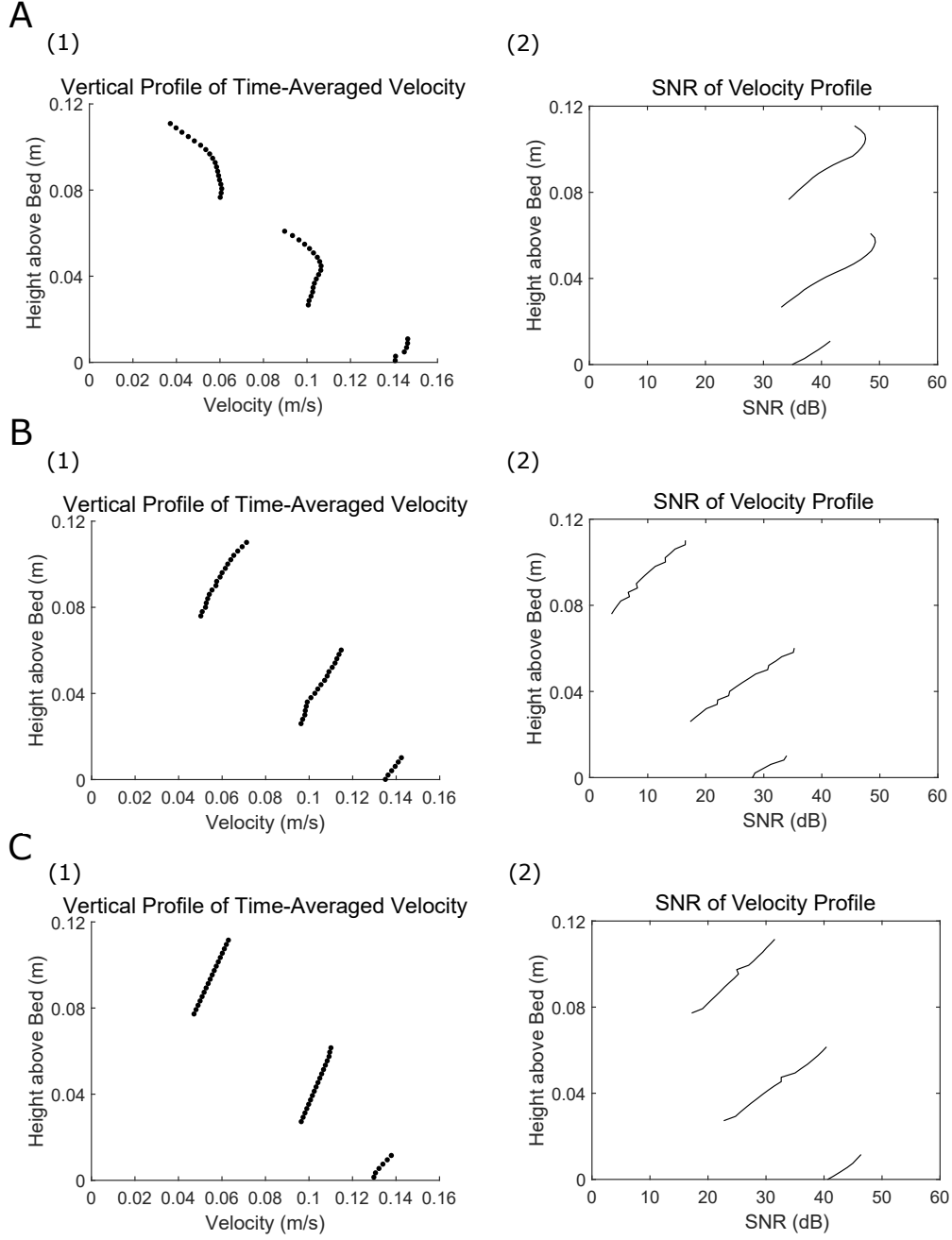


Figure A2. Time-averaged velocity profile and SNR of velocity profile for experiments conducted with 8.00% slope. A. (1) Time-averaged velocity profile of PP3. (2) SNR of velocity profile for PP3. B. (1) Time-averaged velocity profile of PP4. (2) SNR of velocity profile for PP4. C. (1) Time-averaged velocity profile of PP5. (2) SNR of velocity profile for PP5.

B2D). The low $C_{T,0}$, U_0 case had the most sediment deposited toward the upstream end of the flow.

For the both high and low $C_{T,0}$, U_0 simulations, a thicker deposit was observed for grain-size classes 1 and 2 than for grain-size classes 3 and 4 (Figures B1E, G, H and B2E, G, H). Although the initial concentrations of the finer grain-size classes 3 and 4 $C_{3,0}$, $C_{4,0}$ were higher than that of the coarser grain-size class 1 ($C_{1,0}$), less fine sediment was deposited since it was more likely to remain suspended and be carried beyond the lower flow boundary by the high-velocity flow. For the low $C_{T,0}$, U_0 simulation, the coarser grain-size class, grain-size classes 1 and 2, had almost all sediment deposited near the upstream boundary, whereas the finer grain-size class, grain-size classes 3 and 4, had sediment spread out toward the downstream direction (Figures B2E, F, G, H). This happened because the low-velocity flow was unable to keep the coarse sediment suspended.

Table B1. Initial flow conditions of numerical simulations of turbidity currents.

	High $C_{T,0}$, U_0	Low $C_{T,0}$, U_0
H_0 (m)	0.15	0.15
U_0 (m/s)	0.2	0.02
$C_{T,0}$	0.018	0.001
$C_{1,0}$	0.004	0.0002
$C_{2,0}$	0.005	0.0003
$C_{3,0}$	0.0047	0.00027
$C_{4,0}$	0.0043	0.00023
c_f	0.004	0.004
r_o	1.5	1.5
Duration (s)	420	420

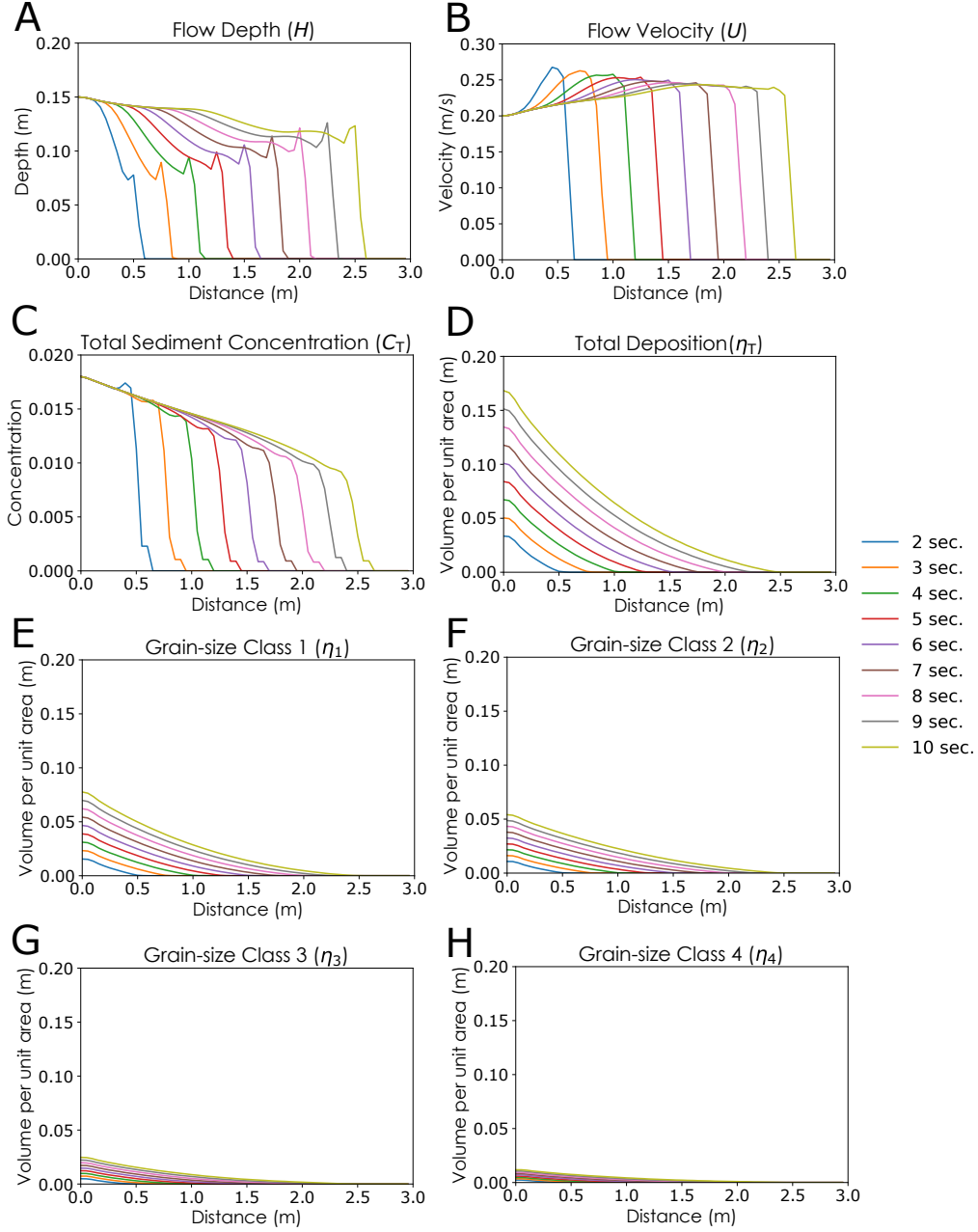


Figure B1. Example of forward model calculation with high initial flow velocity and sediment concentration (Table B1). A. Time evolution of flow depth H . B. Time evolution of flow velocity U . C. Time evolution of total sediment volumetric concentration C_T . D. Time evolution of deposit profile η_T . E. Time evolution deposit profile of grain-size class 1 η_1 . F. Time evolution of deposit profile of grain-size class 2 η_1 . G. Time evolution of deposit profile of grain-size class 3 η_1 . H. Time evolution of deposit profile of grain-size class 4 η_1 .

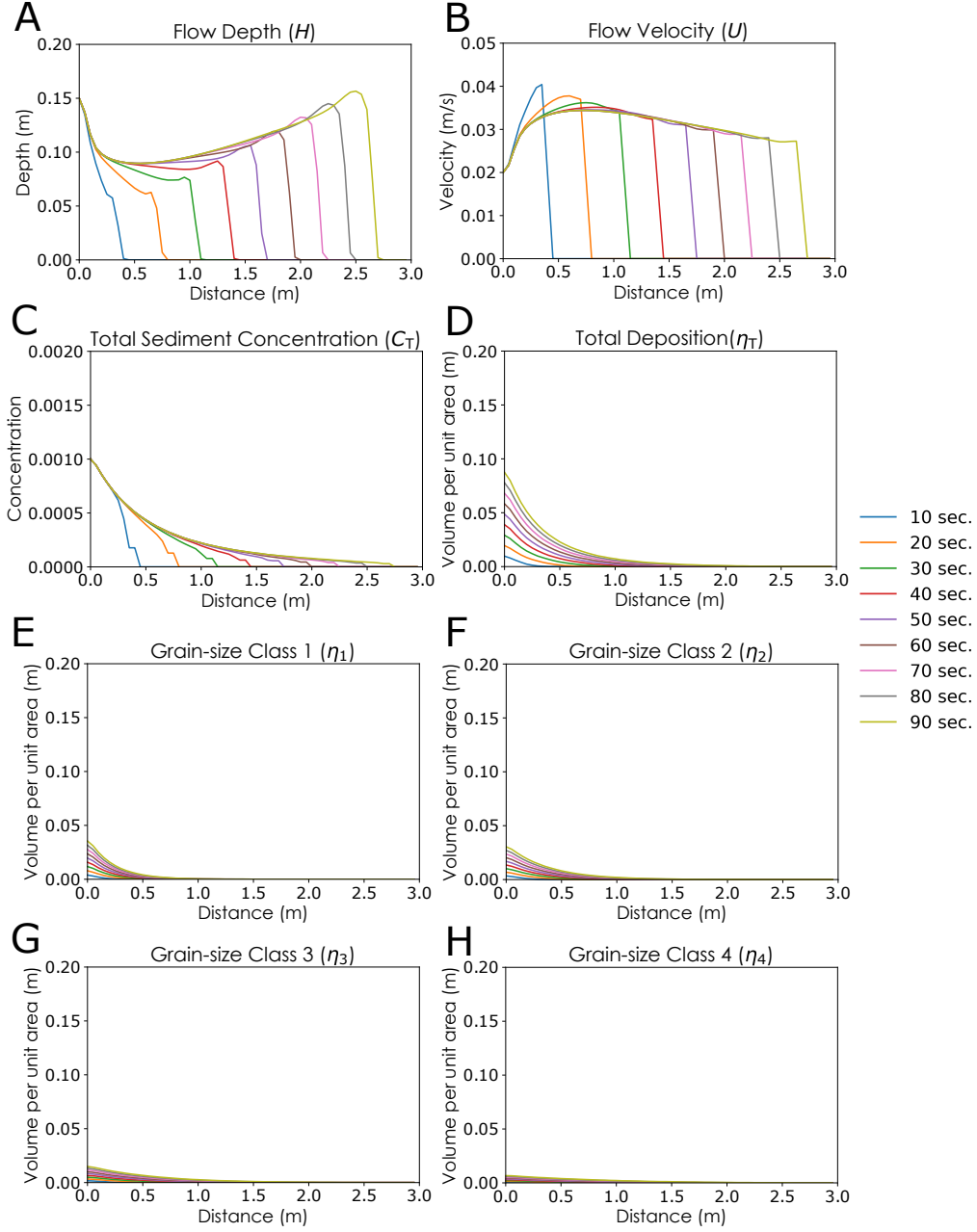


Figure B2. Example of forward model calculation with low initial flow velocity and sediment concentration (Table B1). A. Time evolution of flow depth H . B. Time evolution of flow velocity U . C. Time evolution of total sediment volumetric concentration C_T . D. Time evolution of deposit profile η_T . E. Time evolution deposit profile of grain-size class 1 η_1 . F. Time evolution of deposit profile of grain-size class 2 η_1 . G. Time evolution of deposit profile of grain-size class 3 η_1 . H. Time evolution of deposit profile of grain-size class 4 η_1 .

B2 Sensitivity Tests of Forward Model

The degree of sensitivity of the forward model to changes in the initial conditions of the flow and model parameters was tested (Table B2). Testing was conducted using the forward model programmed for generating numerical datasets of experiments conducted with the 10% slope. Numerical simulations were conducted with different values of the six parameters H_0 , U_0 , $C_{T,0}$, e_s , r_o , and c_f . H_0 , U_0 and $C_{T,0}$ values in Case 1 were the mid-values over the range of H_0 , U_0 , and $C_{T,0}$ for generating training data. Other parameters remained constant for the simulations.

The results of the sensitivity tests revealed that changes in the deposit profile occur when the initial flow conditions differ (Figure B3). The volume of the deposited sediment increased overall as H_0 increased (Figure B3A). The same trend was observed for U_0 , and $C_{T,0}$ (Figure B3B, C). Among these three parameters, the amount of increase in the volume per unit area of deposit was greatest for $C_{T,0}$, and smallest for U_0 and H_0 . Concerning model closure parameters, the resultant deposit profile showed almost no change for different values of entrainment coefficient e_s and c_f (Figure B3D, F). A slightly lower amount of deposition was observed for larger e_s . A small increase in the amount of deposition was observed as c_f decreased (Figure B3F). The volume per unit area of deposit increased moderately when r_o increased.

Table B2. Settings for sensitivity tests of forward model.

Case	H_0 (m)	U_0 (m/s)	$C_{T,0}$	e_s	r_o	c_f
1	0.15	0.1	0.01	GP	1.5	0.004
2	0.3	0.1	0.01	GP	1.5	0.004
3	0.05	0.1	0.01	GP	1.5	0.004
4	0.15	0.2	0.01	GP	1.5	0.004
5	0.15	0.02	0.01	GP	1.5	0.004
6	0.15	0.1	0.02	GP	1.5	0.004
7	0.15	0.1	0.001	GP	1.5	0.004
8	0.15	0.1	0.01	GPx2	1.5	0.004
9	0.15	0.1	0.01	GPx0.5	1.5	0.004
10	0.15	0.1	0.01	GP	2.0	0.004
11	0.15	0.1	0.01	GP	1.0	0.004
12	0.15	0.1	0.01	GP	1.5	0.01
13	0.15	0.1	0.01	GP	1.5	0.007
14	0.15	0.1	0.01	GP	1.5	0.001
15	0.15	0.1	0.01	GP	1.5	0.0005

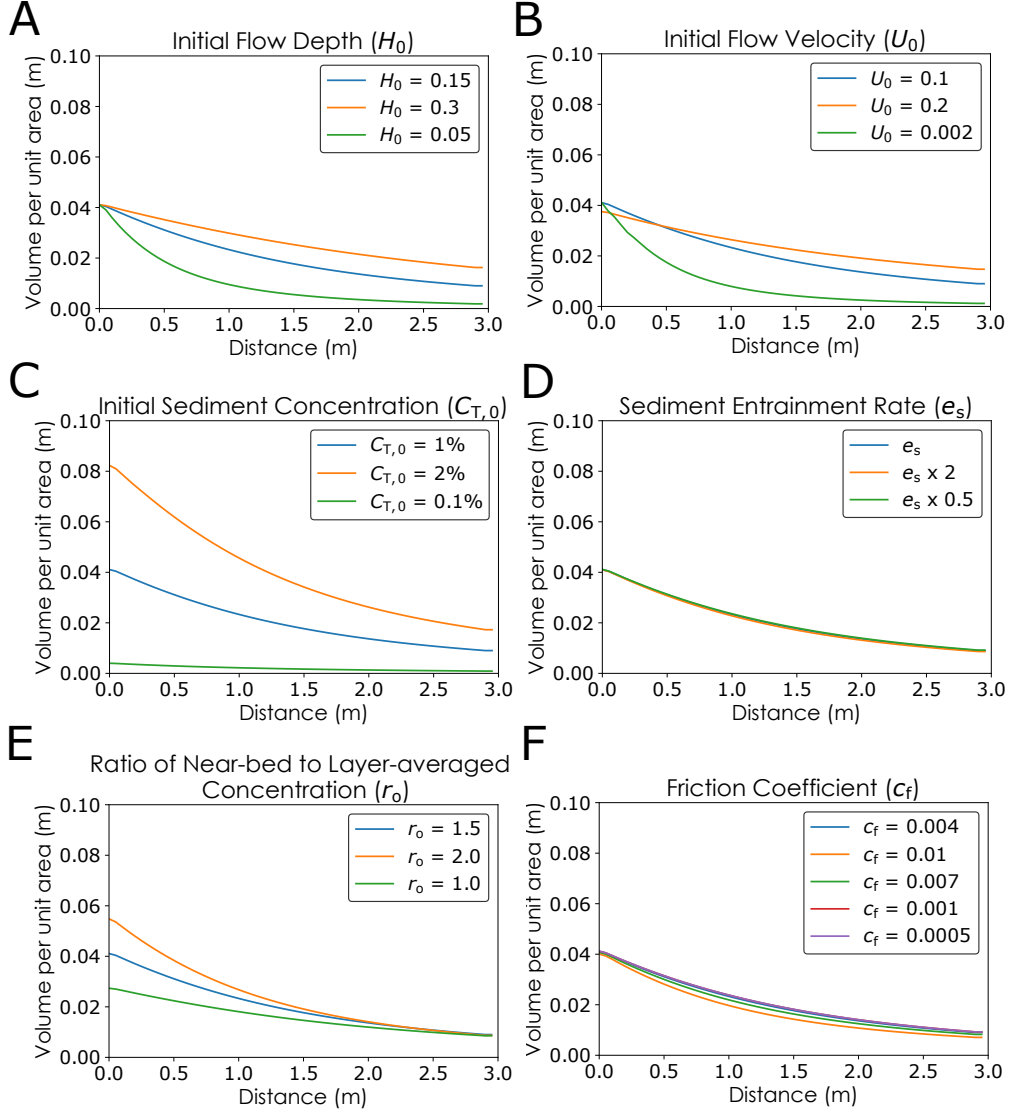


Figure B3. Sensitivity tests of deposit profile of numerical turbidites to change in initial flow conditions and closure parameters (Table B2). A. Dependency on initial flow depth H_0 . B. Dependency on initial flow velocity U_0 . C. Dependency on initial total sediment volumetric concentration $C_{T,0}$. D. Dependency on sediment entrainment rate e_s . E. Dependency on the ratio of near-bed to layer-averaged concentration r_o . F. Dependency on friction coefficient c_f .

B3 Verification of Forward Model with Results from Previous Research

We conducted calculations on experiment NOVA2 (García, 1993) under the same flow conditions and parameter settings as those used for modeling in Kostic and Parker (2006) to validate the numerical scheme and forward model implemented in this study. The resulting flow depth profile, velocity profile and concentration profile were compared with the model results from Kostic and Parker (2006) and the experiment data from García (1993) in Figure B4. The calculated flow depth profile showed an almost perfect match with that from Kostic and Parker (2006) (Figure B4A). The velocity profile was slightly higher than that of Kostic and Parker (2006) before the slope break, with close match for the values after the slope break (Figure B4B). The calculated concentration profile by the model in this study was slightly higher than that of Kostic and Parker (2006) (Figure B4C). The overall reconstruction by the model implemented in this study matched the results from the previous study by Kostic and Parker (2006).

B4 Sensitivity of Forward Model to Different Entrainment Functions

Calculations were conducted using the same initial flow conditions as those of experiments GLASSA5 and GLASSA7 (García, 1993) to test sensitivity of the implemented forward model to different entrainment functions. Three different entrainment functions were tested, including functions from van Rijn (1984), Garcia and Parker (1993), and Dorrell et al. (2018). The resulting deposit profiles are shown in Figure B5. Measurements from García (1993) and model results from Kostic and Parker (2006) are also shown for comparison. Figures B5A and B show that results from the model implemented in this study showed a closer match with the experimental measurements from García (1993), but the deposit profile showed almost no change with the change in entrainment function. A greater difference may be visible for a field scale simulation, but for experimental turbidity currents, the effect does not seem to be visibly large.

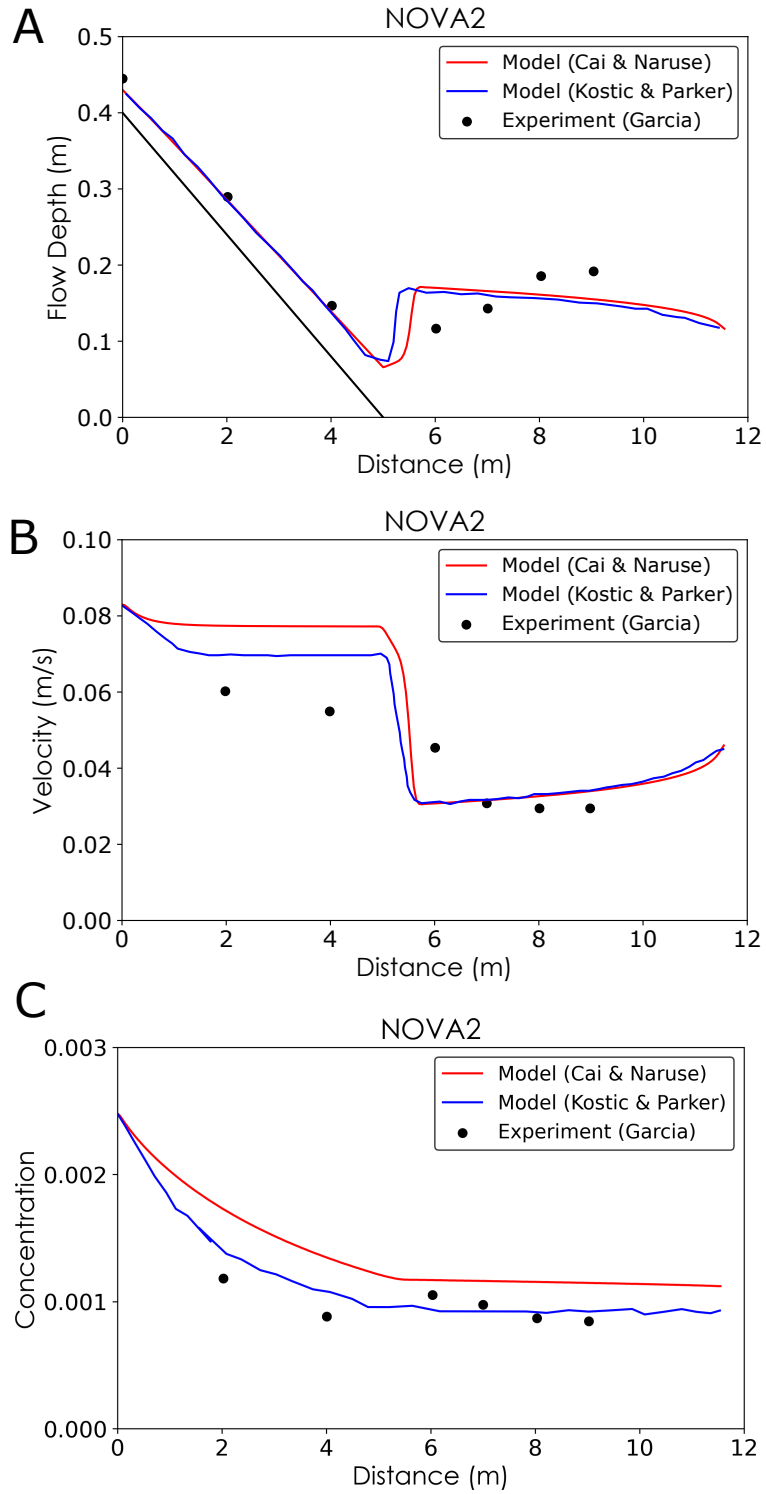


Figure B4. Forward model calculation results using initial flow conditions of experiment NOVA2 from García (1993). Plotted with experimental measurements from García (1993) and model results from Kostic and Parker (2006). A. Flow depth profile. B. Velocity profile. C. Concentration profile

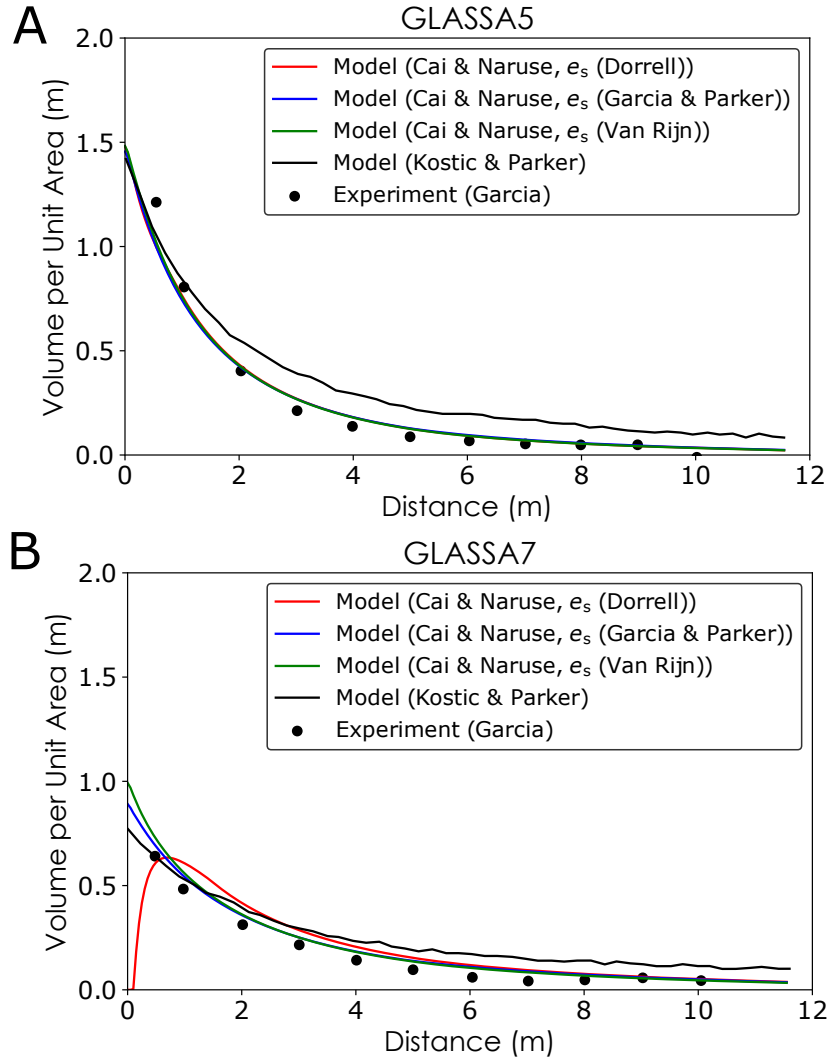


Figure B5. Forward model test of sensitivity to different entrainment functions using initial flow conditions of experiment GLASSA5 and GLASSA7 from (García, 1993). Plotted with experimental measurements from (García, 1993) and model results from Kostic and Parker (2006). A. Deposit profile of GLASSA5 when calculated with different entrainment functions. B. Deposit profile of GLASSA7 when calculated with different entrainment functions.

Notation

α_1, α_2	Parameters related to sediment entrainment
B	Bias
c_f	Friction coefficient
C_i	Layer-averaged volumetric concentration of suspended sediment of the i th grain-size class
CI of B	95% confidence interval of bias
C_s	Discharge coefficient
C_T	Layer-averaged total concentration of suspended sediment
C_v^*	The mid-value over the range in which the specific parameter was generated
D_i	Representative grain diameter of the i th grain-size class
e_{si}	Entrainment rate of sediment of the i th grain-size class into suspension
e_w	Entrainment rate of ambient water to flow
F_i	Volume fraction of the i th grain-size class in active layer
g	Gravitational acceleration
H	flow depth
L_a	Active layer thickness
M	Flow discharge
R	Submerged specific density of sediment
R_{fi}	Dimensionless particle fall velocity of the i th grain-size class
Ri	Bulk Richardson number
Re_{pi}	Particle Reynolds number of the i th grain-size class
r_o	Ratio of near-bed suspended sediment concentration to the layer-averaged concentration of suspended sediment
s	Sample standard deviation
t	Time
T_d	Flow duration
U	Layer-averaged flow velocity
u_*	Shear velocity
w_i	Settling velocity of a sediment particle of the i th grain-size class
x	Streamwise distance
η_i	Volume per unit area of bed sediment of the i th grain-size class
η_T	Total volume per unit area of bed sediment
κ	Parameter related to artificial viscosity
λ_p	Porosity of bed sediment
μ	Dynamic viscosity of water
ν	Kinematic viscosity of water
ρ	Density of water
θ	Angle of inclination of the base slope

Acknowledgments

This work was supported by the Sediment Dynamics Research Consortium (SDRC). DOI for data and code is 10.5281/zenodo.4780814. We would like to thank Enago (<https://www.enago.jp/>) for English language editing.

References

Abadi, M., Agarwal, A., Barham, P., Brevdo, E., Chen, Z., Citro, C., . . . Zheng, X. (2015). *TensorFlow: Large-scale machine learning on heterogeneous sys-*

- tems. Retrieved from <http://tensorflow.org/> (Software available from tensorflow.org)
- Altinakar, M., Graf, W., & Hopfinger, E. (1996). Flow structure in turbidity currents. *Journal of Hydraulic Research*, 34(5), 713-718. Retrieved from <https://doi.org/10.1080/00221689609498467> doi: 10.1080/00221689609498467
- Arai, K., Naruse, H., Miura, R., Kawamura, K., Hino, R., Ito, Y., ... Kasaya, T. (2013, 11). Tsunami-generated turbidity current of the 2011 tohoku-oki earthquake. *Geology*, 41(11), 1195-1198.
- Azpiroz-Zabala, M., Cartigny, M. J. B., Talling, P. J., Parsons, D. R., Sumner, E. J., Clare, M. A., ... Pope, E. L. (2017). Newly recognized turbidity current structure can explain prolonged flushing of submarine canyons. *Science Advances*, 3(10). Retrieved from <https://advances.sciencemag.org/content/3/10/e1700200> doi: 10.1126/sciadv.1700200
- Baas, J. H., Van Dam, R. L., & Storms, J. E. A. (2000). Duration of deposition from decelerating high-density turbidity currents. *Sedimentary Geology*, 136(1), 71-88.
- Biegert, E., Vowinkel, B., Ouillon, R., & Meiburg, E. (2017). High-resolution simulations of turbidity currents. *Progress in Earth and Planetary Science*, 4(1), 33.
- Bottou, L. (2010). Large-scale machine learning with stochastic gradient descent. In Y. Lechevallier & G. Saporta (Eds.), *Proceedings of compstat'2010* (pp. 177-186). Heidelberg: Physica-Verlag HD.
- Bouma, A. H. (1962). *Sedimentology of some flysch deposits: A graphic approach to facies interpretation*. Elsevier.
- Cantero, M. I., Balachandar, S., & Garcia, M. H. (2007). High-resolution simulations of cylindrical density currents. *Journal of Fluid Mechanics*, 590, 437-469.
- Chikita, K. (1989). A field study on turbidity currents initiated from spring runoffs. *Water Resources Research*, 25(2), 257-271. Retrieved from <https://agupubs.onlinelibrary.wiley.com/doi/abs/10.1029/WR025i002p00257> doi: 10.1029/WR025i002p00257
- Daly, R. A. (1936). Origin of submarine canyons. *American Journal of Science*, 31(186), 401-420.
- Davison, A. C., & Hinkley, D. V. (1997). *Bootstrap methods and their application*. Cambridge University Press. doi: 10.1017/CBO9780511802843
- Dietrich, W. E. (1982). Settling velocity of natural particles. *Water Resources Research*, 18(6), 1615-1626. doi: 10.1029/WR018i006p01615
- Dorrell, R. M., Amy, L. A., Peakall, J., & McCaffrey, W. D. (2018). Particle size distribution controls the threshold between net sediment erosion and deposition in suspended load dominated flows. *Geophysical Research Letters*, 45(3), 1443-1452.
- Dorrell, R. M., Darby, S. E., Peakall, J., Sumner, E. J., Parsons, D. R., & Wynn, R. B. (2014). The critical role of stratification in submarine channels: Implications for channelization and long runout of flows. *Journal of Geophysical Research: Oceans*, 119(4), 2620-2641. Retrieved from <https://agupubs.onlinelibrary.wiley.com/doi/abs/10.1002/2014JC009807> doi: 10.1002/2014JC009807
- Dorrell, R. M., Peakall, J., Sumner, E. J., Parsons, D. R., Darby, S. E., Wynn, R. B., ... Tezcan, D. (2016). Flow dynamics and mixing processes in hydraulic jump arrays: Implications for channel-lobe transition zones. *Marine Geology*, 381, 181-193. Retrieved from <http://www.sciencedirect.com/science/article/pii/S0025322716302055> doi: <https://doi.org/10.1016/j.margeo.2016.09.009>
- Falcini, F., Marini, M., Milli, S., & Moscatelli, M. (2009). An inverse problem to infer paleoflow conditions from turbidites. *Journal of Geophysical Research: Oceans*, 114.

- Fukushima, Y., Parker, G., & Pantin, H. M. (1985). Prediction of ignitive turbidity currents in scripps submarine canyon. *Marine Geology*, 67(1), 55–81.
- Garcia, M., & Parker, G. (1991). Entrainment of bed sediment into suspension. *Journal of Hydraulic Engineering*, 117(4), 414–435.
- Garcia, M., & Parker, G. (1993). Experiments on the entrainment of sediment into suspension by a dense bottom current. *Journal of Geophysical Research*, 98(C3), 4793–4807.
- García, M. H. (1993). Hydraulic jumps in sedimen-driven bottom currents. *Journal of Hydraulic Engineering*, 119(10), 1094–1117. Retrieved from <https://ascelibrary.org/doi/abs/10.1061/%28ASCE%290733-9429%281993%29119%3A10%281094%29> doi: 10.1061/(ASCE)0733-9429(1993)119:10(1094)
- Gibbs, R. J. (1974). A settling tube system for sand-size analysis. *Journal of Sedimentary Petrology*, 44(2), 583–588.
- Gunawan, H. P. (2015). *Numerical simulation of shallow water equations and related models* (Theses, Université Paris-Est). Retrieved from <https://tel.archives-ouvertes.fr/tel-01216642>
- Heerema, C. J., Talling, P. J., Cartigny, M. J., Paull, C. K., Bailey, L., Simmons, S. M., ... Pope, E. (2020). What determines the downstream evolution of turbidity currents? *Earth and Planetary Science Letters*, 532, 116023. Retrieved from <http://www.sciencedirect.com/science/article/pii/S0012821X19307150> doi: <https://doi.org/10.1016/j.epsl.2019.116023>
- Jameson, A., Schmidt, W., & Turkel, E. (1981). Numerical solution of the euler equations by finite volume methods using runge kutta time stepping schemes. In *14th fluid and plasma dynamics conference* (p. 1259).
- Johnson, D. W. (1939). *The origin of submarine canyons: A critical review of hypotheses*. Columbia University Press.
- Kostic, S., & Parker, G. (2006). The response of turbidity currents to a canyon–fan transition: Internal hydraulic jumps and depositional signatures. *Journal of Hydraulic Research*, 44(5), 631–653. Retrieved from <https://doi.org/10.1080/00221686.2006.9521713> doi: 10.1080/00221686.2006.9521713
- Krizhevsky, A., Sutskever, I., & Hinton, G. E. (2012). Imagenet classification with deep convolutional neural networks. In F. Pereira, C. J. C. Burges, L. Bottou, & K. Q. Weinberger (Eds.), *Advances in neural information processing systems 25* (pp. 1097–1105). Curran Associates, Inc. Retrieved from <http://papers.nips.cc/paper/4824-imagenet-classification-with-deep-convolutional-neural-networks.pdf>
- Kuenen, P. H., & Migliorini, C. I. (1950). Turbidity currents as a cause of graded bedding. *The Journal of Geology*, 58(2), 91–127.
- Lesshafft, L., Meiburg, E., Kneller, B., & Marsden, A. (2011). Towards inverse modeling of turbidity currents: The inverse lock-exchange problem. *Computers and Geosciences*, 37(4), 521–529. doi: <https://doi.org/10.1016/j.cageo.2010.09.015>
- Liang, S., & Srikant, R. (2016). Why deep neural networks for function approximation? *CoRR*, abs/1610.04161. Retrieved from <http://arxiv.org/abs/1610.04161>
- McIntosh, A. (2016). *The jackknife estimation method*.
- Nakao, K., Naruse, H., & Tokuhashi, S. (2020, 10). Inverse analysis to reconstruct hydraulic conditions of non-steady turbidity currents: Application to an ancient turbidite of the kiyosumi formation of the awa group, boso peninsula, central japan. *EarthArXiv*. Retrieved from <https://eartharxiv.org/repository/view/1715/>
- Naruse, H. (2005). Usage and advantages of an application program “stube” for settling tube grain-size analysis. *Journal of the Sedimentological Society of Japan*, 62(62), 55–61.
- Naruse, H., & Nakao, K. (2020). Inverse modeling of turbidity currents using artificial neural network: verification for field application. *Earth Surface Dynam-*

- ics Discussions, 2020, 1–27. Retrieved from <https://esurf.copernicus.org/preprints/esurf-2020-93/> doi: 10.5194/esurf-2020-93
- Naruse, H., & Olariu, C. (2008). Hydraulic conditions of turbidity currents estimated by inverse analysis. In *Fourth international conference on scour and erosion* (pp. 591–593). Japanese Geotechnical Society.
- Nielsen, M. A. (2015). *Neural networks and deep learning*. Determination Press.
- Parker, G., Garcia, M., Fukushima, Y., & Yu, W. (1987). Experiments on turbidity currents over an erodible bed. *Journal of Hydraulic Research*, 25(1), 123–147.
- Parkinson, S. D., Funke, S. W., Hill, J., Piggott, M. D., & Allison, P. A. (2017). Application of the adjoint approach to optimise the initial conditions of a turbidity current with the adjointturbidity 1.0 model. *Geoscientific Model Development*, 10(3), 1051–1068.
- Paull, C. K., Talling, P. J., Maier, K. L., Parsons, D., Xu, J., Caress, D. W., ... Cartigny, M. J. (2018). Powerful turbidity currents driven by dense basal layers. *Nature Communications*, 9(1), 4114.
- Pradhan, B., Lee, S., & Buchroithner, M. F. (2010). A gis-based back-propagation neural network model and its cross-application and validation for landslide susceptibility analyses. *Computers, Environment and Urban Systems*, 34(3), 216–235.
- Rogers, S. J., Fang, J. H., Karr, C. L., & Stanley, D. A. (1992). Determination of lithology from well logs using a neural network. *AAPG Bulletin*, 76(5), 731–739.
- Ruder, S. (2016). An overview of gradient descent optimization algorithms. *CoRR*, abs/1609.04747. Retrieved from <http://arxiv.org/abs/1609.04747>
- Rumble, J. R. (2018). *Crc handbook of chemistry and physics, 99th edition*. CRC Press.
- Schmidhuber, J. (2015). Deep learning in neural networks: An overview. *Neural Networks*, 61, 85–117. Retrieved from <http://www.sciencedirect.com/science/article/pii/S0893608014002135> doi: <https://doi.org/10.1016/j.neunet.2014.09.003>
- Simmons, S. M., Azpiroz-Zabala, M., Cartigny, M. J. B., Clare, M. A., Cooper, C., Parsons, D. R., ... Talling, P. J. (2020). Novel acoustic method provides first detailed measurements of sediment concentration structure within submarine turbidity currents. *Journal of Geophysical Research: Oceans*, 125(5), e2019JC015904. Retrieved from <https://agupubs.onlinelibrary.wiley.com/doi/abs/10.1029/2019JC015904> doi: 10.1029/2019JC015904
- Talling, P. J., Allin, J., Armitage, D. A., Arnott, R. W. C., Cartigny, M. J. B., Clare, M. A., ... Xu, J. (2015). Key future directions for research on turbidity currents and their deposits. *Journal of Sedimentary Research*, 85(2), 153–169.
- Talling, P. J., Amy, L. A., & Wynn, R. B. (2007). New insight into the evolution of large-volume turbidity currents: Comparison of turbidite shape and previous modelling results. *Sedimentology*, 54(4), 737–769.
- Talling, P. J., Masson, D. G., Sumner, E. J., & Malgesini, G. (2012). Subaqueous sediment density flows: Depositional processes and deposit types. *Sedimentology*, 59(7), 1937–2003.
- Vangriesheim, A., Khripounoff, A., & Crassous, P. (2009). Turbidity events observed in situ along the congo submarine channel. *Deep Sea Research Part II: Topical Studies in Oceanography*, 56(23), 2208–2222.
- van Rijn, L. C. (1984). Sediment transport, part ii: Suspended load transport. *Journal of Hydraulic Engineering*, 110(11), 1613–1641. Retrieved from <https://ascelibrary.org/doi/abs/10.1061/%28ASCE%290733-9429%281984%29110%3A11%281613%29> doi: 10.1061/(ASCE)0733-9429(1984)110:11(1613)
- Vestbøstad, T. M., Faltinsen, O. M., Kristiansen, D., et al. (2007). Validation methods and benchmark tests for a 2-d cip method applied to marine hydrodynamics. In *The seventeenth international offshore and polar engineering*

- conference.
- Wang, Z., & Bovik, A. C. (2009). Mean squared error: Love it or leave it? a new look at signal fidelity measures. *IEEE Signal Processing Magazine*, 26(1), 98–117. doi: 10.1109/MSP.2008.930649
- Weimer, P., & Slatt, R. M. (2007). Introduction to the petroleum geology of deepwater settings. *AAPG Studies in Geology*, 57, 149-227.
- Xu, J. P., Noble, M. A., & Rosenfeld, L. K. (2004). In-situ measurements of velocity structure within turbidity currents. *Geophysical Research Letters*, 31(9).
- Yabe, T., Xiao, F., & Utsumi, T. (2001). The constrained interpolation profile method for multiphase analysis. *Journal of Computational Physics*, 169(2), 556–593.
- Yang, H., Lu, M., & Kumakura, T. (2016). A study on the water front in shallow water equations. *Journal of Japan Society of Civil Engineers, Ser. B1 Hydraulic Engineering*, 72(4), I325-I330. doi: 10.2208/jscejhe.72.I_325